Energy Conversion and Management 260 (2022) 115616

Contents lists available at ScienceDirect

Energy Conversion and Management

journal homepage: www.elsevier.com/locate/enconman

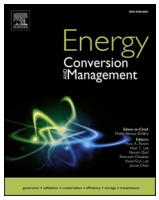

Thermodynamic assessment of a geothermal power and cooling cogeneration system with cryogenic energy storage

Tuğberk Hakan Çetin [a], Jie Zhu [a,*], Ekrem Ekici [b], Mehmet Kanoglu [c]

[a] Department of Architecture and Built Environment, University of Nottingham, University Park, Nottingham NG7 2RD, UK
[b] Department of Engineering, University of Cambridge, Trumpington Street, Cambridge CB2 1PZ, UK
[c] Department of Mechanical Engineering, Alanya Alaaddin Keykubat University, Alanya, Antalya, Turkey

ARTICLE INFO

Keywords:
Combined power and cooling
Energy storage
Cryogenics
Geothermal energy
Liquid air

ABSTRACT

Geothermal energy is one of the main renewable energy sources for power generation and district cooling, and liquid air energy storage is an emerging technology suitable for both power and cold storages. Accordingly, a combined power and cooling cogeneration system with cryogenic energy storage is proposed in this paper, which is powered by geothermal energy and connected with the grid. The system is formed by integrating a turbine ejector cogeneration cycle with an air liquefaction cycle, a liquid air direct expansion cycle and a cryogenic organic Rankine cycle. In normal operation mode, only the turbine ejector cogeneration cycle works in the system based on the cooling load requirement. In charging operation mode, all the power produced in the system is used to liquefy air in the air liquefaction cycle owing to cheap electricity tariff. In discharging operation mode, the additional electricity is provided to meet peak time energy requirement by the direct expansion cycle and cryogenic organic Rankine cycle. A geothermal source at 180 °C with a flow rate of 100 kg/s is used as the heat source in this study, the cogeneration system has the ability to produce 15,470 kW of power and supply 4800 kW of cooling simultaneously, the system round trip efficiency is 41.07%, and the exergy efficiency of cryogenic energy storage is 60.43%. Also, the effects of geothermal energy temperature, system size, turbine mass split ratio and normalized mass flow rate on the system performance are clarified.

1. Introduction

Currently, buildings consume around 40% of the primary energy and contribute about 36% of greenhouse gas emissions in the EU [1,2], and most of the energy is used to meet heating and cooling demands [3]. These demands can be fulfilled by district energy facilities with a central energy source resulting in low carbon emissions [4,5]. The district energy systems could be powered by renewable energy sources [6], such as biomass, solar and geothermal energy, etc. Among them, the geothermal energy is a promising energy source for district heating/cooling applications due to its high potential and independent nature on weather condition [7,8]. Yilmaz [9] investigated the performance of an absorption chiller powered by a 100 °C geothermal energy source to meet cooling demand of 232 apartments in Izmir, Turkey, and found that the COP and payback period of the chiller are 0.441 and 5.68 years, respectively. Tugcu et al. [10] optimized a NH_3-H_2O absorption cycle driven by geothermal energy based on artificial neural networks, and achieved a COP of 0.572 and an exergy efficiency of 62.0% with a 133.5 °C geothermal energy source at a flow rate of 462 kg/s. Similar to the absorption cooling system, the ejector-based cooling system can also be powered by geothermal energy, but it has lower initial cost and higher reliability compared with the absorption cooling system [11]. Therefore, the ejector-based system is a favorable way to use geothermal energy for cooling.

A number of studies have been conducted on the combined power and cooling systems powered by geothermal energy. Nami et al. [12] proposed a geothermal combined cooling, heating and power (CCHP) system which consists of an organic Rankine Cycle (ORC), a LiBr–H_2O absorption chiller and a heat exchanger to provide space heating and domestic hot water. With a 105 °C geothermal heat source, the power and cooling output of the system are 232.6 kW and 1058 kW respectively in summer, and its heating capacity is 6029 kW in winter. The system maximum exergy efficiencies are 59.5% and 68.2% for the summer and winter periods, respectively. Mosaffa et al. [13] carried out thermodynamic and economic analyses of a CCHP cycle, which consists of a ejector based cooling unit, an ORC and a domestic water heating system. In the optimum configuration, an energy efficiency of 85.3%

* Corresponding author.
E-mail address: jie.zhu@nottingham.ac.uk (J. Zhu).

https://doi.org/10.1016/j.enconman.2022.115616
Received 9 March 2022; Received in revised form 2 April 2022; Accepted 10 April 2022
Available online 20 April 2022

Nomenclature

CES	cryogenic energy storage
CORC	cryogenic organic Rankine cycle
$\dot{E}x$	exergy (kW)
ex	specific exergy (kJ/kg)
g	mass of air liquefied per mass of geothermal water
h	specific enthalpy(kJ/kg)
HX	heat exchanger
I	irreversibility (kW)
J-T	Joule-Thompson
LNG	liquefied natural gas
$\dot{m}$	mass flow rate (kg/s)
$\dot{Q}$	heat transfer rate (kW)
r	mass flow rate ratio (%)
S	entropy (kW/K)
T	temperature (°C or K)
TES	thermal energy storage
W	power (kW)
w	specific work (kJ/kg)
y	liquid yield (%)

Greek letters

α	mass of CORC working fluid per liquid air
β	mass of CORC working fluid per geothermal water
μ	entrainment ratio
γ_p	mass of power fraction of working fluid per geothermal water
γ_r	mass of cooling fraction of working fluid per geothermal water
γ	normalized total mass flow rate
τ	ratio of mass flow rate of high pressure turbine exit to mass flow rate of ejector primary flow
Δ	difference
ε	exergy efficiency
η	energy efficiency

Subscripts and indices

1,2,3..	states
bin	binary
ces	cryogenic energy storage
cry	cryogenic
ejec	ejector
evap	evaporator
geo	geothermal
liq	liquefaction
rt	round-trip
turb	turbine
m	mixing
n	nozzle
d	diffuser
s	isentropic
p	power
r	refrigeration

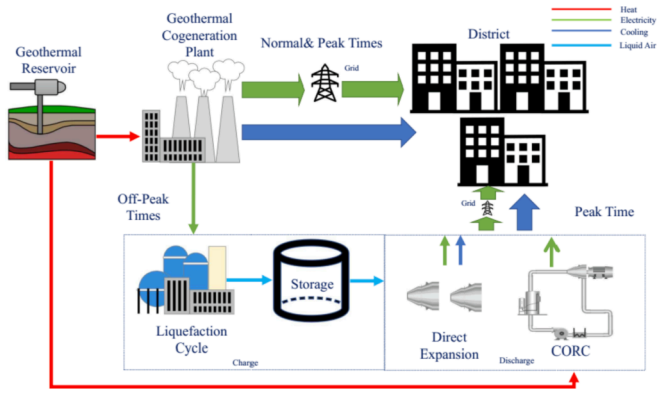

Fig. 1. Geothermal power and cooling generation with CES.

and an exergy efficiency of 67.7% of the cycle are achieved. Zare et al. [14] proposed two novel CCHP systems with an ejector CO_2 *trans*-critical cycle based on Rankine cycle with and without internal heat exchanger. The two configurations have power output of 17.2 kW and 25.6 kW, and thermal efficiencies of 43.8% and 39.8%, respectively. Ipakchi et al. [15] conducted a thermoeconomic and parametric study to evaluate energy performance of an ejector based *trans*-critical CO_2 combined cooling and power generation system. They found the system generates 10 kW cooling and 7.55 kW power with the optimal energy efficiency of 27.4% and exergy efficiency 24.2%. Casanova et al. [16] developed a supercritical CO_2 power generation cycle with low-grade geothermal heat source, and investigated different cycle configurations. They claimed that the intercool recuperated Brayton cycle is the most feasible cycle with 780 kW power output, 11.51% energy efficiency and 52.49% exergy efficiency.

Increases in renewable energy penetration and highly transient characteristics of power and heating/cooling demands lead to integration of energy storage [17]. Cryogenic Energy Storage (CES) and Liquid Air Energy Storage (LAES) are the promising energy storage options to meet the peak period power demand and provide additional flexibility for renewable energy application. Unlike the pumped hydro and compressed air energy storage systems, the CES is not constrained by geographical location [18–20]. During the off peak period, the excessive electricity is used to power air liquefaction cycle for producing liquid air. During the peak period, the liquid air is heated either by the stored thermal energy in the compression process or by the available waste heat to produce additional electricity for meeting the peak demand. The CES system can be utilized alone or integrated with another energy systems [21,22].

Multi-generation systems with the CES have been proposed in recent years for high energy conversion efficiency. Taffone et al. [23] developed a stand-alone LAES multi-generation system to supply electricity and chilled water. With a 5 °C turbine outlet temperature, their system reaches around 45% round-trip efficiency. He et al. [24] proposed a cascaded utilization of Liquefied Natural Gas (LNG) to power a CES integrated ORC system in a data center, and they noted that the system can produce 103 kW electricity and 217 kW cooling in the optimum configuration. Gao et al. [25] carried out thermodynamic, economic and thermo-economic analyses of a tri-generation system based on stand-alone LAES, and found that the system has round trip efficiencies of 55.41%, 55.35% and 54.68% for winter, transition, and summer seasons, respectively. Bosch et al. [26] designed a stand-alone LAES system to run under a cogeneration regime. The liquid air and turbine outlet air are utilized in a three-way heat exchanger to provide cooling during discharge period, and the system reaches a round trip efficiency of 41.9%. Mugnini [27] investigated the cold exergy in a district cooling system, and discovered that around 60% of the electricity savings can be achieved by utilizing the LNG. Zhang et al. [28] proposed a cryogenic thermoelectric generator for recovering available cryogenic energy during discharging operation, and found that the decoupled LAES system reaches a round trip efficiency of 29% and a combined power and cooling efficiency of 50%.

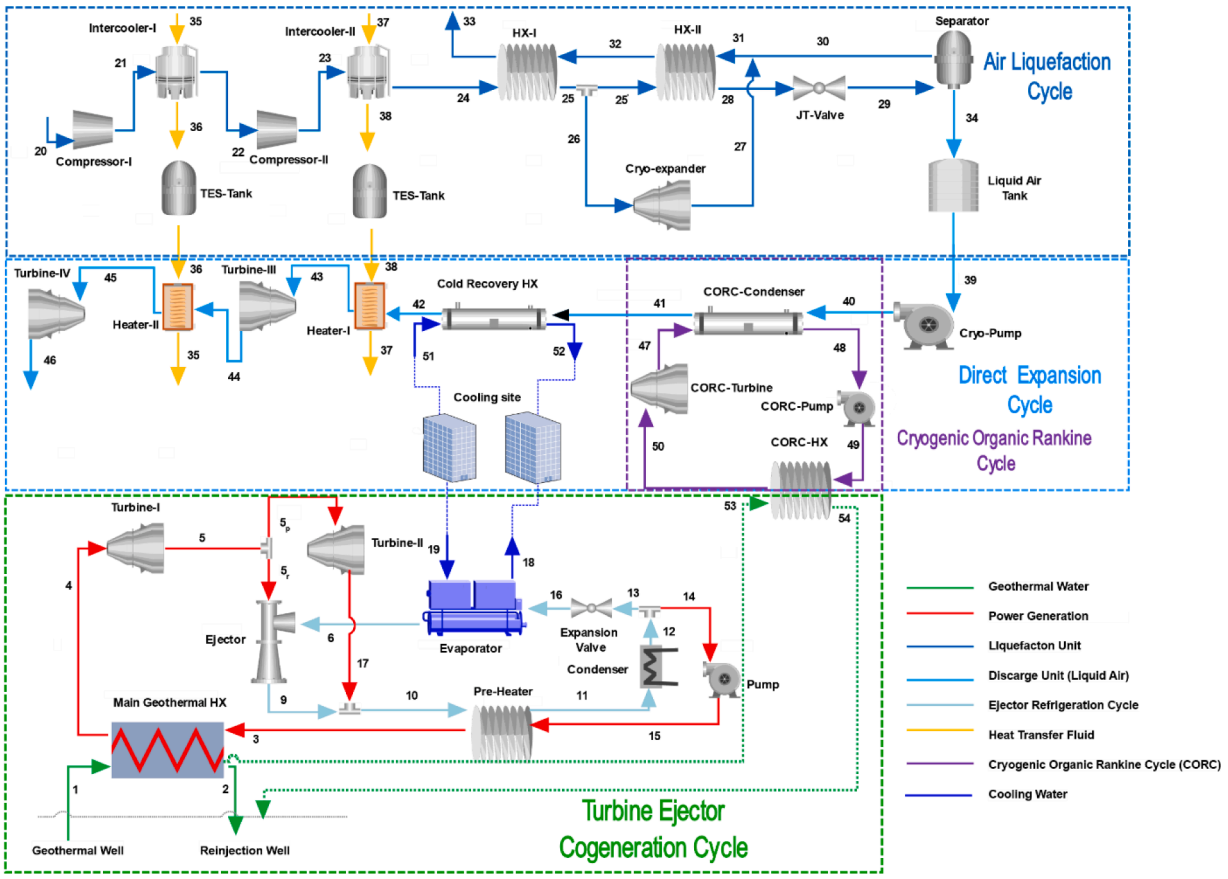

Fig. 2. Schematic representation of the geothermal power and cooling cogeneration system with CES.

Unlike other renewable energy sources such as wind and solar, geothermal energy is always available, but as renewable energy penetration increases throughout the grid, the flexible power generation is getting more important to match varying demands. Thus, integration of energy storage in the geothermal energy system is one of the promising solutions for power plant to operate under high varying demands.

The synergic operation of geothermal power and cooling cogeneration system and the CES has not been explored until now, in order to fill this research gap, a novel geothermal cogeneration system integrated with the CES is investigated in this study, which has the ability to provide high flexible power and cooling output (Fig. 1). The system is formed by integrating a turbine ejector cogeneration cycle with an air liquefaction cycle, a liquid air direct expansion cycle and a Cryogenic Organic Rankine Cycle (CORC). Thermodynamic assessment of the system from first and second law aspects is carried out for three operating modes, the parametric studies are conducted to clarify the effects of the heat source temperature, system size, turbine mass split ratio and normalized mass flow rate on the system performance. The proposed system performance is also compared with the similar energy systems with the CES and CORC to justify efficiency and specific work output.

2. System description and operation

As presented in Fig. 2, the proposed system is formed by integrating a turbine ejector cogeneration cycle with a CES plant. The system operates in three modes: normal, charging and discharging modes. In the normal operation mode, only the turbine ejector cogeneration cycle runs to produce power and cooling simultaneously. In the charging mode, all of generated electricity by the turbine ejector cycle is supplied to the air liquefaction cycle to produce liquefied air. In the discharging mode, the stored liquid air is discharged to produce additional cooling and electricity along with the turbine ejector cogeneration cycle and CORC.

2.1. Turbine ejector cogeneration cycle

The turbine ejector cogeneration cycle consists of a main geothermal heat exchanger, a high and a low pressure turbines (Turbines I and II), an evaporator, a preheater, a condenser and a pump. CO_2 is selected as the working fluid due to its characteristics, such as environmental friendliness, wide availability, thermal stability and low critical point (31.0 °C and 73.8 bar). The low critical point feature enables the utilization of its supercritical properties for power generation while providing considerable amount of cooling [29]. At first, the CO_2 is heated in the main geothermal heat exchanger and expands in the high pressure Turbine I for power generation. The middle pressure CO_2 from Turbine I is separated into two streams: one is directed into the low pressure Turbine II to expand for more power generation (state 5_p) while the other is guided into the ejector as the primary fluid (state 5_r) for cooling production. In the ejector, the primary fluid entrains the secondary fluid from the evaporator (state 6), then they leave the ejector and merge with the stream from Turbine II to form the low pressure working fluid. Afterwards, the low pressure working fluid is condensed in the condenser after being cooled in the preheater. Then the low pressure working fluid is split into two parts again. The first stream flows through the throttling valve and into the evaporator to produce cooling effect while the second stream goes through a pump to increase its pressure and then enters the preheater and main heat exchanger to complete the cycle at last.

2.2. Cryogenic energy storage plant

The CES plant has three cycles: an air liquefaction cycle operating in charging operation mode; a direct liquid air expansion cycle and a CORC

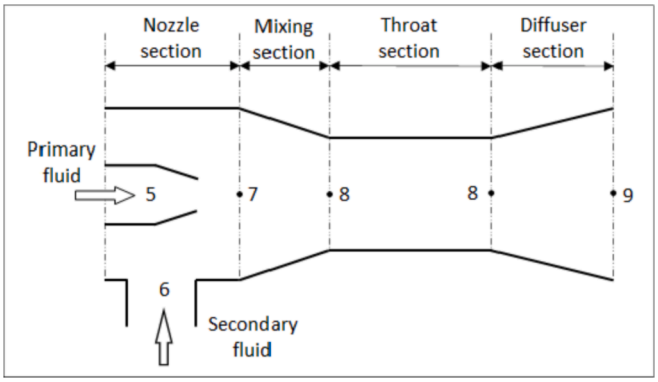

Fig. 3. Ejector internal structure.

operating in discharging operation mode. The air liquefaction cycle is a Kapitza cycle-based liquefaction system which consists of two compressors (I and II), two intercoolers, two thermal energy storage (TES) tanks, two heat exchangers (HX- I and HX-II), one cryo-expander, one expansion valve and one storage tank. During charging operation, the ambient air pressure is increased by two compressors (I and II) with an intercooler and an aftercooler. The recovered thermal energy from both the coolers is stored in two TES tanks separately by thermal fluid Dowtherm T [30]. The high pressure air is consecutively cooled in the two heat exchangers (HX-I and HX-II), one portion of the high pressure air from HX-I is diverted through the cryo-expander to decrease the air temperature and then mixes with upcoming air from the separator. The high pressure and low temperature air from HX-II rapidly expands through a Joule-Thomson valve and then gets into the separator. The liquid portion of the expanded air in the separator is collected in the storage tank while the gas portion is utilized to cool the high-pressure air in the two heat exchangers.

The direct liquid air expansion cycle includes a cryo-pump, a CORC-condenser (shared), a cold recovery heat exchanger, two heaters and two turbines. Propane is selected as the working fluid in the CORC owing to its low condensing temperature [31]. During the discharging operation, the stored liquid air is discharged and pumped to reach a higher pressure, and then it is used to cool the working fluid in the CORC condenser, and recover cold in the cold recovery heat exchanger. Afterwards, it is heated in Heaters I and II and expands in Turbine III and IV respectively. The CORC consists of a condenser (shared with the direct liquid air expansion cycle), a turbine, a pump and a heat exchanger. The CORC is also powered by geothermal water leaving the main geothermal HX, the heated propane expands in the CORC turbine, then is condensed by the discharged liquid air and pumped into the CORC-HX by the CORC-pump to complete the cycle.

3. Thermodynamic analyses

The system has the complex structure, in order to simplify the system mathematical models, the following assumptions are adopted [32–34]:

(1) The system operates under steady state.
(2) Pressure drops in pipes and heat losses to the environment are neglected.
(3) The specific enthalpies before and after the throttle valve are the same.
(4) The outlet working fluids of the evaporators and condensers are saturated vapor and saturated liquid, respectively.
(5) The flow inside the ejector is in steady state with one-dimension.
(6) The ejector inlet velocities of the primary and secondary fluids are negligible.
(7) Preheater and main geothermal heat exchanger are sized to maintain the minimum temperature differences for both charging and discharging operations [35].

The analyses of the system are performed quantitively and qualitatively based on the first and second laws of thermodynamics, respectively [34]. Fundamental governing equations used in this study are stated as follows:

$$\sum \dot{m}_i = \sum \dot{m}_e \tag{1}$$

$$\sum \dot{Q} - \sum \dot{W} = \sum \dot{m}_e h_e - \sum \dot{m}_i h_i \tag{2}$$

$$\sum S_i - \sum S_e + S_{gen} = 0 \tag{3}$$

$$\sum \dot{E}x_Q - \dot{W} = \sum \dot{m}\, ex_e - \sum \dot{m}\, ex_i + I_{rev} \tag{4}$$

where $\dot{m}$ denotes the mass flow rate of the fluid, $\dot{Q}$ and $\dot{W}$ are the rates of heat input and power output, h is the specific enthalpy, $\dot{E}x$ is the exergy rate and I is the irreversibility rate. The exergy of heat transfer at temperature T can be expressed as [36]:

$$\dot{E}x_{heat} = \sum (1 - \frac{T_0}{T})\dot{Q} \tag{5}$$

The specific exergy of each fluid stream is.

$$ex = (h - h_0) - T_0(s - s_0) \tag{6}$$

where *0* subscript stands for the dead state of corresponding thermodynamic property.

3.1. Ejector model

The ejector consists of the nozzle, mixing, throat and diffuser sections, as shown in Fig. 3. The ejector analysis is conducted based on conservation laws of mass, momentum, and energy [32]. The outlet velocity of the primary fluid from the nozzle V_7 is formulated as:

$$V_7 = \sqrt{2\eta_n(h_5 - h_{7,s})} \tag{7}$$

where η_n is the nozzle isentropic efficiency, $h_{7,s}$ is the outlet enthalpy of isentropic flow.

The ejector entrainment ratio μ is defined as:

$$\mu = \frac{\dot{m}_6}{\dot{m}_{5r}} \tag{8}$$

where $\dot{m}_{5r}$ is the primary mass flow rate and $\dot{m}_6$ is the secondary mass flow rate.

The ideal outlet velocity of the mixing section can be expressed as:

$$V_{8,s} = \frac{V_7}{1+\mu} \tag{9}$$

The mixing efficiency of the mixing section is.

$$\eta_m = \frac{V_8^2}{V_{8,s}^2} \tag{10}$$

The velocity of the mixed fluid can be calculated as:

$$V_8 = \sqrt{\eta_m}\ \frac{V_7}{1+\mu} \tag{11}$$

In the mixing section, its energy conservation equation can be expressed as:

$$\dot{m}_7(h_7 + \frac{V_7^2}{2}) + \dot{m}_6(h_6 + \frac{V_6^2}{2}) = (\dot{m}_6 + \dot{m}_7)(h_8 + \frac{V_8^2}{2}) \tag{12}$$

In the diffuser section, the actual enthalpy h_9 at the diffuser outlet is.

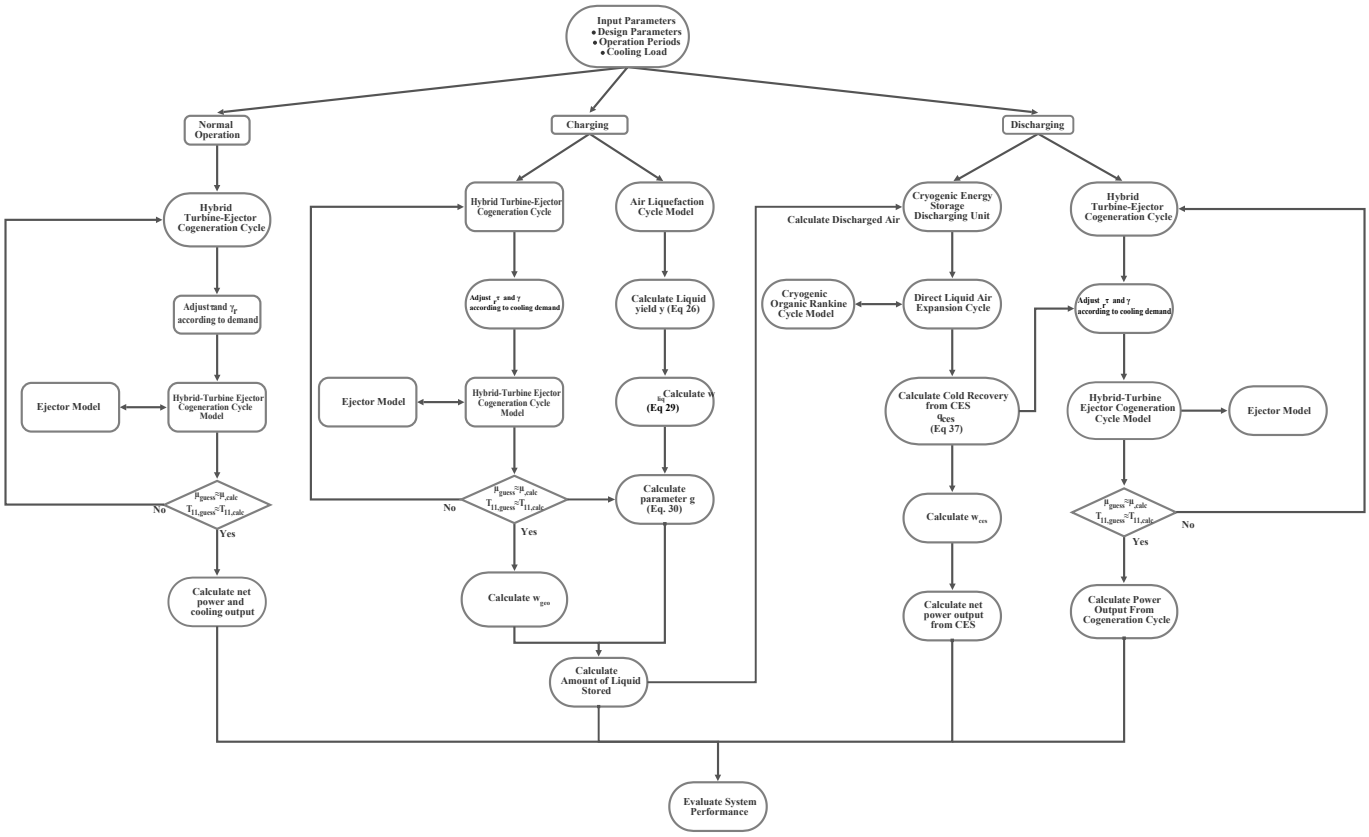

Fig. 4. Calculation workflow for proposed study.

Table 1
Comparison of ejector model results with literature [14] data.

State	Literature[14]			Proposed Study			Difference (%)
	P (MPa)	T (°C)	h (kJ/kg)	P (MPa)	T (°C)	h (kJ/kg)	
Primary Flow Inlet	7.6	42.68	−81.55	7.6	42.68	−81.55	
Secondary Flow Inlet	3.969	5	−79.29	3.969	5	−79.29	
Primary Nozzle Outlet	3.969	5	−100.1	3.969	5	−100.1	0
Mixing Flow	3.969	5	−93.47	3.969	5	−93.8	−0.35305
Ejector Outlet	5.5	22.74	−81.27	5.5	22.74	−81.27	0
Entrainment ratio	0.1379			0.1427			−3.48078

Table 2
Comparison of obtained results of current study with literature [32] data.

Performance Parameter	This Study	Wang's Study [32]	Difference (%)
High Pressure Turbine specific work (kJ/kg)	18.61	18.36	1.3617
Low Pressure Turbine specific work (kJ/kg)	13.8	13.42	2.8316
Specific Pump Work (kJ/kg)	0.555	0.55	0.9091
Refrigeration Output (kW)	21.65	21.015	3.0217
Main Heat Exchanger Duty (kW)	938.1	905.688	3.5787
Thermal Efficiency (%)	15.08	14.92	1.0724

$$h_9 = h_8 + \frac{h_{9,s} - h_8}{\eta_d} \tag{13}$$

where η_d is the diffuser efficiency.

3.2. Turbine ejector cogeneration cycle model

The mass flowrates at the diverted states 13 and 14 are normalized with respect to the main geothermal heat exchanger mass flow rate by defining the mass flow ratio diverted to the power section γ_p, and diverted to the cooling section γ_r,as follows:

$$\gamma_p = \frac{\dot{m}_{14}}{\dot{m}_1} \tag{14}$$

$$\gamma_r = \frac{\dot{m}_{13}}{\dot{m}_1} \tag{15}$$

The normalized total mass flow rate γ of the turbine ejector cogeneration cycle is the sum of γ_p and γ_r, it indicates the size of the system and is expressed as:

Table 3
Parameters used in the present study [14,18,31,38].

Parameter	Value
Minimum Temperature Difference in liquefaction unit ΔT_{min} (°C)	1
Minimum Temperature Difference in intercoolers & heaters ΔT_{min} (°C)	1
Minimum Temperature Difference in CORC units ΔT_{min} (°C)	1
Minimum Temperature Difference in main heat exchanger (°C)	5
Compressor outlet pressure of liquefaction unit P_{23} (kPa)	4000
Cryo-expander flow rate ratio r	0.76
Charging operation duration (h)	6
Discharging operation duration (h)	1
Isentropic efficiency of compressors	0.85
Isentropic efficiency of ejector turbines and cryo-expander	0.9
Isentropic efficiency of CES direct expansion turbines	0.85
Isentropic efficiency of cryo-pump and CORC pump	0.85
Isentropic efficiency of ejector pump	0.9
Nozzle Isentropic Efficiency in Ejector	0.9
Mixing Isentropic Efficiency in Ejector	0.88
Diffuser Isentropic Efficiency in Ejector	0.85
Evaporator Temperature (°C)	6
Dead State Pressure (kPa)	101.325
Dead State Pressure (°C)	25
γ (kg working fluid/kg geothermal water)	1.5
Refrigeration Output (kW)	4800

Table 4
Thermodynamic properties of dead states of working fluids.

Fluid	*P* (kPa)	*T* (C)	*h* (kJ/kg)	*s* (kJ/kg K)
Air	101.325	25	298.4	6.859
Water	101.325	25	104.9	0.3672
Propane	101.325	25	630.7	2.846
Dowtherm T	101.325	25	68.18	0.2372
CO_2	101.325	25	−0.9383	−0.002199

$$\gamma = \gamma_r + \gamma_p = \frac{\dot{m}_{12}}{\dot{m}_1} \tag{16}$$

Another important parameter for the turbine ejector cogeneration cycle is the turbine mass split ratio τ, which is the ratio of the mass flow rate of the low pressure turbine II to the mass flow rate diverted to the power section, and expressed as:

$$\tau = \frac{\dot{m}_{5r}}{\dot{m}_{14}} \tag{17}$$

The specific work produced by the high-pressure and low-pressure turbines can be expressed as:

$$w_{ejec,turb} = (h_4 - h_5) + (1-\tau)(h_5 - h_{17})(\text{kJ/kg working fluid}) \tag{18}$$

The specific pump power consumption in the cycle is.

$$w_{ejec,pump} = (h_{15} - h_{14})(\text{kJ/kg working fluid}) \tag{19}$$

The net work output from the turbine-ejector cogeneration cycle is the difference between the turbine work output and pump input power:

$$w_{ejec,net} = w_{ejec,turb} - w_{ejec,pump}(\text{kJ/kg working fluid}) \tag{20}$$

The specific cooling output of the cogeneration cycle is given by:

$$q_{ejec,evap} = (h_6 - h_{16})(\text{kJ/kg working fluid}) \tag{21}$$

Equations (20) and (21) can also be written in terms of geothermal water flow rate with the help of parameters γ_p and γ_r. The specific work and cooling produced in terms of geothermal water flow rate can be written as:

$$w_{geo} = \gamma_p w_{ejec,net}(\text{kJ/kg geothermal water}) \tag{22}$$

$$q_{geo} = \gamma_r q_{ejec,evap}(\text{kJ/kg geothermal water}) \tag{23}$$

Finally, the thermal and exergy efficiencies of the turbine ejector cogeneration cycle can be expressed as:

$$\eta_{th} = \frac{w_{geo} + q_{geo}}{q_{in}} = \frac{w_{geo} + q_{geo}}{h_1 - h_2} \tag{24}$$

Table 6
Performance data for normal operation.

Parameter	Value
γ_p	1.247
γ_r	0.253
τ	0.3965
μ	0.5121
q_{in}(kJ/kg geothermal water)	314.2
$w_{ejec,net}$ (kJ/kg CO_2)	39.56
w_{geo} (kJ/kg geothermal water)	49.33
$\dot{W}_{ejec}$ (kW)	4933
$q_{ejec,evap}$(kJ/kg CO_2)	189.6
$q_{geo,evap}$(kJ/kg geothermal water)	48
$\eta_{thermal}$ (%)	30.97
ε_{ejec} (%)	59.38

Table 5
Stream data of normal operation.

State	Substance	$\dot{m}$ (kg/s)	*P* (kPa)	*T* (°C)	*h* (kJ/kg)	*s* (kJ/kg.K)	*ex* (kJ/kg)	$\dot{E}x$ (kW)
1	Water	100	1003	180	763.1	2.139	129.8	12,980
2	Water	100	1003	106.9	448.8	1.383	40.91	4091
3	CO_2	124.7	15,000	54.97	−177.1	−1.355	227.2	28,330
4	CO_2	124.7	15,000	175	74.92	−0.6809	278.2	34,688
5	CO_2	124.7	8000	118.8	37.42	−0.6702	237.5	29,619
5_p	CO_2	75.27	8000	118.8	37.42	−0.6702	237.5	17,876
5_r	CO_2	49.43	8000	118.8	37.42	−0.6702	237.5	11,741
6	CO_2	25.31	3969	5	−79.29	−0.9227	196.1	4964
7	CO_2	49.43	3969	63.05	1.015	−0.6581	197.5	9764
8	CO_2	74.75	3969	48.35	−16.12	−0.7102	195.9	14,644
9	CO_2	74.75	5000	68.42	−2.11	−0.7041	208.1	15,554
10	CO_2	150	5000	74.45	5.169	−0.6829	209.1	31,360
11	CO_2	150	5000	27.14	−60.31	−0.8864	204.2	30,637
12	CO_2	150	5000	14.28	−268.9	−1.61	211.4	31,714
13	CO_2	25.31	5000	14.28	−268.9	−1.61	211.4	5352
14	CO_2	124.7	5000	14.28	−268.9	−1.61	211.4	26,362
15	CO_2	124.7	15,000	26.14	−255.9	−1.606	223.2	27,826
16	CO_2	25.31	3969	5	−268.9	−1.604	209.7	5309
17	CO_2	75.25	5000	80.55	12.4	−0.6623	210.2	15,814

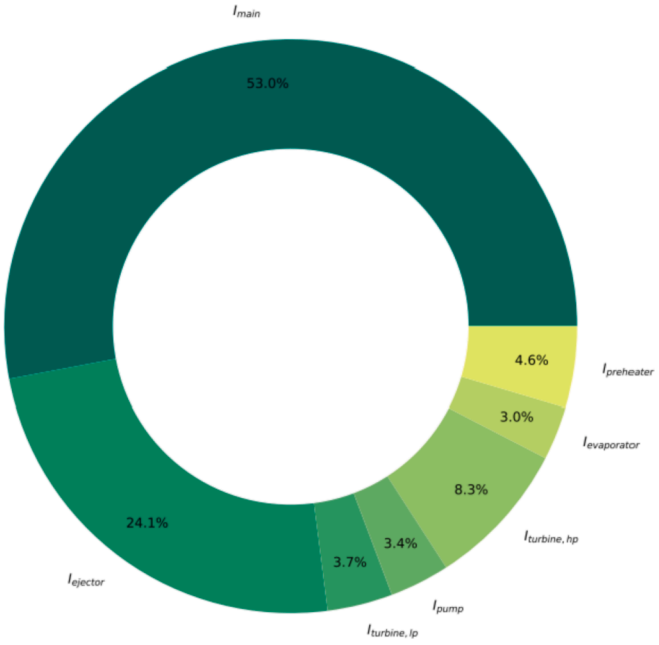

Fig. 5. Proportional irreversibility distribution during normal operation.

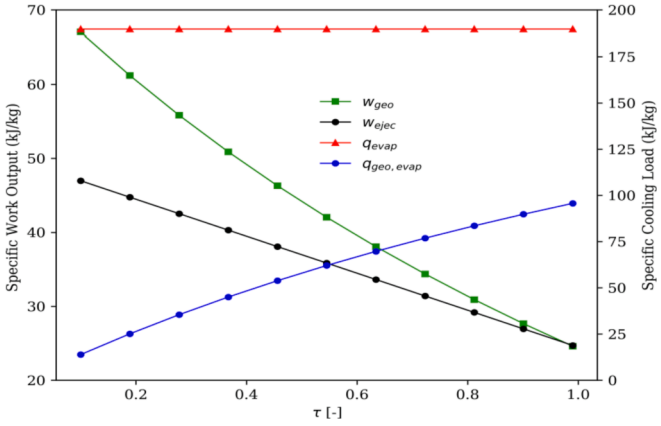

Fig. 6. Variations of specific work output and cooling output with turbine mass split ratio.

$$\varepsilon_{ejec} = \frac{\dot{W}_{ejec,net} + \dot{E}x_{evap}}{\dot{E}x_{geo}} = \frac{w_{geo} + \gamma_r(ex_{16} - ex_6)}{ex_1 - ex_2} \tag{25}$$

3.3. Air liquefaction cycle model

Two performance parameters of the air liquefaction cycle are liquid yield and liquefaction work. At first, the liquid yield is given by.

$$y = \frac{h_{33} - h_{24}}{h_{33} - h_{34}} + r\left(\frac{h_{26} - h_{27}}{h_{33} - h_{34}}\right) \tag{26}$$

where *r* is the fraction of the air diverted through the cryo-expander:

$$r = \frac{\dot{m}_{26}}{\dot{m}_{25}} \tag{27}$$

The power consumption of the liquefaction cycle is.

$$w_{net} = (h_{21} - h_{20}) + (h_{23} - h_{22}) - r(h_{26} - h_{27})(\text{kJ/kg gas}) \tag{28}$$

The liquefaction work per unit mass of the liquefied air can be determined from.

$$w_{liq} = \frac{w_{net}}{y}(\text{kJ/kg liquid air}) \tag{29}$$

The parameter *g* is defined as the mass of liquid air produced per unit of geothermal water entering the system:

$$g = \frac{w_{geo}}{w_{liq}} = \gamma_p \frac{w_{ejec,net}}{w_{liq}}(\text{kg liquid air/kg geothermal water}) \tag{30}$$

3.4. CORC and direct liquid air expansion cycle models

During the discharge operation, the extra power is produced by the CORC and direct liquid air expansion cycle. The net work produced in the CORC per unit liquid air is expressed as:

$$w_{corc} = \alpha((h_{50} - h_{47}) - (h_{49} - h_{48}))(\text{kJ/kg liquid air}) \tag{31}$$

where α is the unit mass of the CORC working fluid per unit mass of the liquid air entering the cycle [31].

$$\alpha = \frac{\dot{m}_{47}}{\dot{m}_{40}}(\text{kg CORC working fluid / kg liquid air}) \tag{32}$$

The thermal efficiency of the CORC can be expressed as:

$$\eta_{CORC} = \frac{\dot{W}_{CORC}}{\dot{Q}_{geo}} = \beta_{cry}\frac{(h_{50} - h_{47}) - (h_{49} - h_{48})}{h_{53} - h_{54}} \tag{33}$$

where β_{cry} is the unit mass of the CORC working fluid per unit mass of geothermal water [31].

The work output from the direct liquid air expansion cycle is.

$$w_{ces-exp} = (h_{43} - h_{44}) + (h_{45} - h_{46}) - (h_{40} - h_{39}) \tag{34}$$

The total specific net work output from the cryogenic energy storage is.

$$w_{ces} = w_{corc} + w_{ces-exp}(\text{kJ/kg liquid air}) \tag{35}$$

The round trip efficiency can be expressed as:

$$\eta_{rt} = \frac{w_{ces} + q_{ces}}{w_{liq}} \tag{36}$$

where q_{ces} is the recovered cold energy from the cryogenic energy storage plant and can be formulated as:

$$q_{ces} = h_{42} - h_{41} \tag{37}$$

The round trip efficiency can also be expressed by power consumption during charging period and energy release during discharging period:

$$\eta_{rt} = \frac{(\dot{W}_{ces} + \dot{Q}_{ces})t_{disc}}{\dot{W}_{liq}t_{cha}} \tag{38}$$

To determine the exergy efficiency during discharge period, the exergy inputs from liquid air, geothermal water and heat recovery fluid are considered. Then, it is expressed as:

$$\varepsilon_{CES} = \frac{\dot{W}_{CORC} + \dot{W}_{ces} + \dot{E}x_{cold,rec}}{\dot{E}x_{in}} \tag{39}$$

where $\dot{E}x_{in}$ is the sum of exergy inputs from the geothermal water, heaters I and II, and liquid air exergy at inlet state. $\dot{E}x_{cold,rec}$ is the cold exergy recovered in the cold recovery HX.

3.5. Calculation procedures and cooling scenario

The integrated system is modelled in Engineering Equation Solver (EES), the calculation procedure in this study is given in Fig. 4. The system is modeled in terms of nondimensionalized parameters to investigate system operation as a whole. In the turbine ejector cogeneration cycle, geothermal water mass flow rate, geothermal source

Table 7
Stream data of charging operation.

State	Substance	$\dot{m}$ (kg/s)	P (kPa)	T (°C)	h (kJ/kg)	s (kJ/kg.K)	ex (kJ/kg)	$\dot{E}x$ (kW)	
1	Water	100	1003	180	763.1	2.139	129.8	12,980	Geothermal Water
2	Water	100	1003	106.9	448.8	1.383	40.91	4091	
3	CO_2	124.7	15,000	54.97	−177.1	−1.355	227.2	28,330	Turbine Ejector Cogeneration Cycle
4	CO_2	124.7	15,000	175	74.92	−0.6809	278.2	34,688	
5	CO_2	124.7	8000	118.8	37.42	−0.6702	237.5	29,619	
5_p	CO_2	75.27	8000	118.8	37.42	−0.6702	237.5	17,876	
5_r	CO_2	49.43	8000	118.8	37.42	−0.6702	237.5	11,741	
6	CO_2	25.31	3969	5	−79.29	−0.9227	196.1	4964	
7	CO_2	49.43	3969	63.05	1.015	−0.6581	197.5	9764	
8	CO_2	74.75	3969	48.35	−16.12	−0.7102	195.9	14,644	
9	CO_2	74.75	5000	68.42	−2.11	−0.7041	208.1	15,554	
10	CO_2	150	5000	74.45	5.169	−0.6829	209.1	31,360	
11	CO_2	150	5000	27.14	−60.31	−0.8864	204.2	30,637	
12	CO_2	150	5000	14.28	−268.9	−1.61	211.4	31,714	
13	CO_2	25.31	5000	14.28	−268.9	−1.61	211.4	5352	
14	CO_2	124.7	5000	14.28	−268.9	−1.61	211.4	26,362	
15	CO_2	124.7	15,000	26.14	−255.9	−1.606	223.2	27,826	
16	CO_2	25.31	3969	5	−268.9	−1.604	209.7	5309	
17	CO_2	75.25	5000	80.55	12.4	−0.6623	210.2	15,814	
18	Water	81.85	850	6	26.07	0.09131	3.401	278.3	District Cooling Water
19	Water	81.85	850	20	84.71	0.2963	0.928	75.96	
20	Air	12.26	101.3	25	298.4	6.859	0	0	Air Liquefaction
21	Air	12.26	636.6	264.1	541.6	6.929	222.3	2726	
22	Air	12.26	636.6	25	297.2	6.328	157.1	1927	
23	Air	12.26	4000	265.1	541.7	6.398	380.7	4668	
24	Air	12.26	4000	25	289.8	5.778	313.7	3847	
25	Air	12.26	4000	−63.31	191.6	5.386	332.3	4074	
26	Air	9.32	4000	−63.31	191.6	5.386	332.3	3097	
27	Air	9.32	101.3	−191.1	79.1	5.542	173.2	1614	
28	Air	2.943	4000	−186.7	−108.9	3.131	704.1	2072	
29	Air	2.943	101.3	−194	−108.9	3.203	682.7	2009	
30	Air	0.2468	101.3	−191.4	78.74	5.538	174.1	42.97	
31	Air	9.567	101.3	−191.1	79.09	5.542	173.2	1657	
32	Air	9.567	101.3	−101	171.5	6.306	38.04	363.9	
33	Air	9.567	101.3	24	297.4	6.855	0.001691	0.01618	
34	Air	2.696	101.3	−194.2	−126.1	2.978	732.6	1975	
35	Dowtherm T	5.339	200	19	56.61	0.1965	0.5674	3.03	Intercooler I
36	Dowtherm T	5.339	200	261	618.1	1.579	149.8	799.8	
37	Dowtherm T	5.528	200	19	56.61	0.1965	0.5674	3.137	Intercooler II
38	Dowtherm T	5.528	200	260	615.4	1.574	148.6	821.4	
55	Water	747.4	850	20	84.71	0.2963	0.928	693.6	Condenser
56	Water	747.4	850	10	42.85	0.151	2.386	1783	

Table 8
Performance data for charging operation.

Parameter	Value
γ_p	1.247
γ_r	0.253
τ	0.3965
μ	0.5121
q_{in}(kJ/kg geothermal water)	314.2
$w_{ejec,net}$ (kJ/kg CO_2)	39.56
w_{geo} (kJ/kg geothermal water)	49.33
$\dot{W}_{ejec}$ (kW)	4933
$q_{ejec\text{-}evap}$(kJ/kg CO_2)	189.6
$q_{geo,evap}$(kJ/kg geothermal water)	48
w_{net} (kJ/kg gas)	402.3
w_{liq} (kJ/kg liquid air)	1829
Liquid yield y (%)	21.99
g	0.02696
$\eta_{thermal}$ (%)	30.97
ε_{ejec} (%)	59.38

temperature and normalized mass flow rate γ are specified. For a given cooling load, turbine mass split ratio τ and mass flow ratio diverted to the cooling section γ_r are calculated. Value of γ_r is constrained by the ejector entrainment ratio μ. Based on these values, the specific work output of the turbine ejector cogeneration cycle w_{geo} can be obtained. In the air liquefaction cycle, compressor outlet pressure, the minimum approach temperature in the heat exchanger and mass flow rate diverted to the cryo-turbine are selected as the design parameters, then liquefaction work w_{liq} and work consumption per unit mass of liquid air w_{geo} are obtained, furthermore the produced liquid air per unit of geothermal water g is gotten. As for the direct expansion cycle and CORC, the specific work output w_{ces} and cooling output q_{ces} are worked out based on specified approach temperatures in heat exchangers. During discharge operation, the cooling output produced by the cold recovery unit of the CES plant $\dot{Q}_{ces}$ and net power output of the CES plant $\dot{W}_{ces}$ are gotten. The remaining portion of the cooling demand is provided by the turbine ejector cogeneration cycle, the turbine mass split ratio and the mass flow ratio diverted to the cooling section γ_r are obtained.

System size and operation are selected on hypothetical cooling scenario for 600 houses with average 100 m^2 floor area each house and average cooling demand of 80 W/m^2 in İzmir, Turkey [37]. In this hypothetical case, the turbine-ejector cogeneration cycle is specified to supply 4800 kW cooling demand. During charging period, it's assumed that all of the electricity output of the turbine ejector cogeneration cycle is supplied to the air liquefaction cycle [31,38]. During discharging period, the cooling demand is met by the CES, cold recovery heat exchanger and the turbine-ejector cogeneration cycle.

4. Model validation

Firstly, the developed ejector model is validated by comparing the

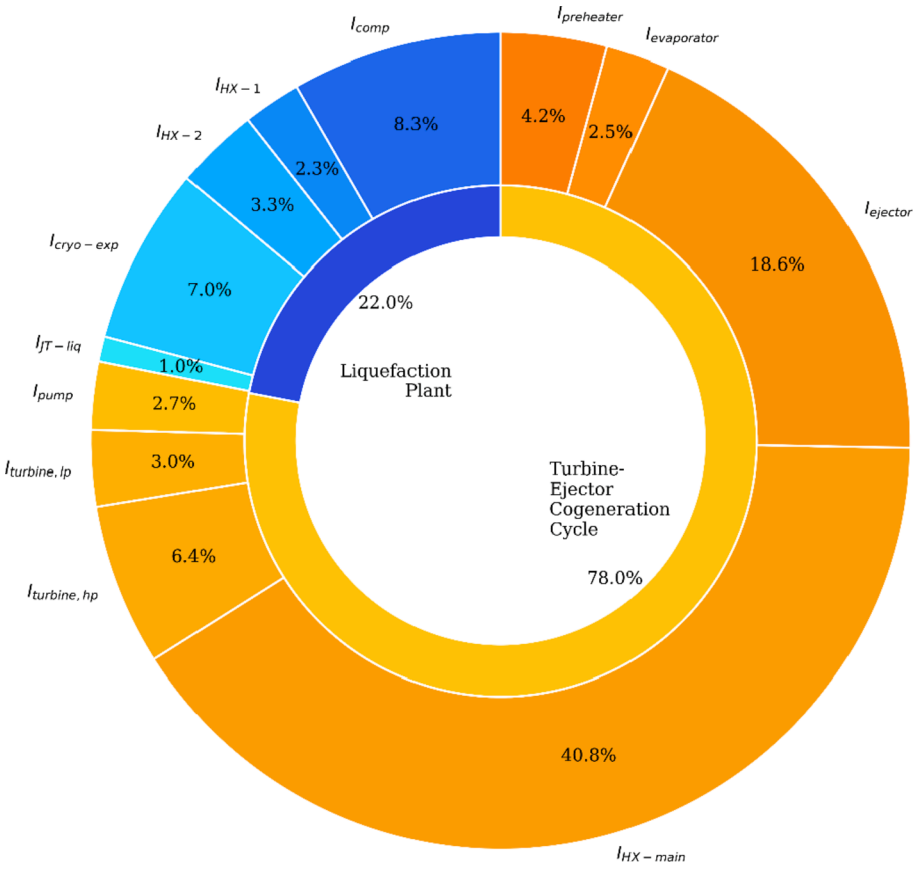

Fig. 7. Proportional irreversibility distribution during charging operation.

simulation results with the data in literature [14], the same operating conditions are used for data comparison purpose, the validation results are presented in Table 1. It can be seen from Table 1 that the maximum difference is 3.48% for the ejector entrainment ratio.

Secondly, the developed model of the turbine ejector cogeneration cycle is verified by the data in literature [32], the results are obtained with a 140 °C heat source at a flow rate of 20 kg/s. The maximum deviation is 3.58% as shown in Table 2.

These comparisons demonstrate the accuracy of the developed models, therefore the models can be used to predict the system performance under various operating conditions.

5. Results and discussion

The system performance under three operating modes (normal, charging and discharging) are investigated, and the effects of the main system parameters involving system size, source temperature, turbine mass split ratio and cold recovery rate on the system power and cooling output are explored.

5.1. Performance evaluation

The system is powered by a 180 °C geothermal source at a flow rate of 100 kg/s, the normalized total mass flow rate γ is taken as 1.5 to evaluate the influence of system size. The working fluid flow rates in the power and cooling cycles are defined by the parameters γ_p in the power section and γ_r in the cooling section in charging and discharging operation modes. The values taken and assumed for the system operation are given in Table 3. The dead state properties of the working fluids are shown in Table 4.

5.1.1. Normal operation

In normal operating mode, the turbine ejector cogeneration cycle runs in stand-alone manner. In this case, the cycle meets the district cooling demand 4800 kW for 17 h by adjusting turbine mass split ratio and mass flow ratio diverted to the cooling section. According to the demand scenario, the cogeneration cycle can also produce 83.3 MWh electricity output during daily normal operation period. The steam data of the normal operation is given in Table 5 and the system performance data is presented in Table 6.

The exergy destruction evaluation is used to determine the lost work potential. Proportional irreversibility distribution in normal operation is given in Fig. 5, the biggest exergy destruction contributor is main heat exchanger accounting of 53% of the total exergy destruction, the next one is the ejector contributing to 24.1% of the total exergy destruction. The main irreversibility sources of the ejector are pure mixing, kinetic energy losses and normal shock wave [39].

The variations of the specific power and cooling output with the turbine mass split ratio are given in Fig. 6. For the evaporation temperature of 5 °C, the specific cooling duty per unit mass of CO_2 remains constant at 189.6 kJ/kg. The ejector motive fluid mass flow rate increases with the turbine mass split ratio, so the ejector can entrain more gas from the evaporator, both the mass flow rate ratio diverted to the cooling section γ_r and cooling output per unit mass of geothermal water rises. The specific cooling load per geothermal water increases from 13.86 kJ/kg to 95.68 kJ/kg when the turbine mass split ratio changes from 0 to 1. Even though enthalpy difference for the cogeneration cycle's turbines remains constant for all cases, the specific work output decreases from 46.98 kJ/kg to 24.71 kJ/kg as the turbine mass split ratio increases from 0 to 1. At the same time, the specific work output per unit mass of geothermal water decreases sharply from 67.4 kJ/kg to 24.60 kJ/kg since it is affected by increase in the turbine mass split ratio τ and decrease in mass flow ratio diverted to the power section γ_p.

Table 9
Stream data of discharging operation.

State	Substance	$\dot{m}$ (kg/s)	P (kPa)	T (°C)	h (kJ/kg)	s (kJ/kg.K)	ex (kJ/kg)	$\dot{E}x$ (kW)	
1	Water	100	1003	180	763.1	2.139	129.8	12,980	Geothermal water
2	Water	100	1003	94.77	397.8	1.247	30.56	3056	
3	CO_2	142.4	15,000	53.59	−181.6	−1.369	226.8	32,300	Turbine Ejector Cogeneration Cycle
4	CO_2	142.4	15,000	175	74.92	−0.6809	278.2	39,618	
5	CO_2	142.4	8000	118.8	37.42	−0.6702	237.5	33,820	
5_p	CO_2	127.57	8000	118.8	37.42	−0.6702	237.5	30,297	
5_r	CO_2	14.83	8000	118.8	37.42	−0.6702	237.5	3522	
6	CO_2	7.594	3969	5	−79.29	−0.9227	196.1	1489	
7	CO_2	14.83	3969	63.05	1.015	−0.6581	197.5	2929	
8	CO_2	22.42	3969	48.35	−16.12	−0.7102	195.9	4393	
9	CO_2	22.42	5000	68.42	−2.11	−0.7041	208.1	4666	
10	CO_2	150	5000	78.71	10.23	−0.6685	209.8	31,472	
11	CO_2	150	5000	27.14	−60.31	−0.8864	204.2	30,637	
12	CO_2	150	5000	14.28	−268.9	−1.61	211.4	31,714	
13	CO_2	7.594	5000	14.28	−268.9	−1.61	211.4	1606	
14	CO_2	142.4	5000	14.28	−268.9	−1.61	211.4	30,109	
15	CO_2	142.4	15,000	26.14	−255.9	−1.606	223.2	31,780	
16	CO_2	7.594	3969	5	−268.9	−1.604	209.7	1593	
17	CO_2	127.6	5000	80.55	12.4	−0.6623	210.2	26,810	
18	Water	24.55	850	6	26.07	0.09131	3.401	83.5	District Cooling Water
19	Water	24.55	850	20	84.71	0.2963	0.928	22.79	
35	Dowtherm T	7.173	200	19	56.61	0.1965	0.5674	4.07	Heater II
36	Dowtherm T	7.173	200	261	618.1	1.579	149.8	1074	
37	Dowtherm T	8.02	200	19	56.61	0.1965	0.5674	4.551	Heater I
38	Dowtherm T	8.02	200	260	615.4	1.574	148.6	1192	
39	Air	16.18	101.3	−194.2	−126.1	2.978	732.6	11,850	CES Expansion Unit
40	Air	16.18	18,000	−188.2	−102.3	3.02	743.7	12,030	
41	Air	16.18	18,000	−109.8	48.62	4.271	521.9	8442	
42	Air	16.18	18,000	17.57	256.3	5.236	441.8	7147	
43	Air	16.18	18,000	259	533.4	5.935	510.5	8258	
44	Air	16.18	1350	17.81	288.2	6.082	221.4	3581	
45	Air	16.18	1350	260	537.1	6.704	284.9	4608	
46	Air	16.18	101.3	24.5	297.9	6.857	0.00043	0.006956	
47	Propane	5.251	2.888	−100	441.4	2.678	−139.1	−730.6	Cryogenic Organic Rankine Cycle
48	Propane	5.251	2.888	−100	−23.59	−0.007878	196.5	1032	
49	Propane	5.251	2500	−99.14	−19.03	−0.003946	199.9	1050	
50	Propane	5.251	2500	93.75	701.4	2.511	170.7	896.2	
51	Water	57.29	850	20	84.71	0.2963	0.928	53.17	District Cooling Water
52	Water	57.29	850	6	26.07	0.09131	3.401	194.8	
53	Water	100	1003	94.77	397.8	1.247	30.56	3056	Geothermal water
54	Water	100	1003	85.77	360	1.143	23.77	2377	
55	Water	747.4	850	20	84.71	0.2963	0.928	693.6	Condenser
56	Water	747.4	850	10	42.85	0.151	2.386	1783	

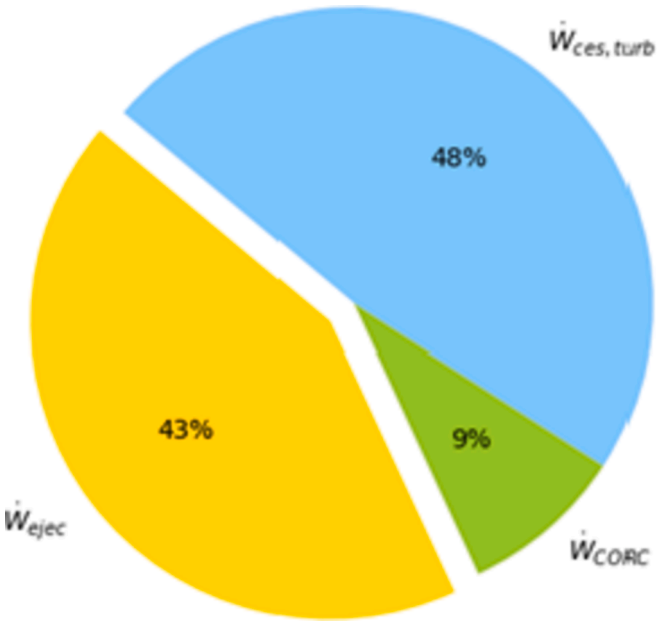

Fig. 8. Distribution of generated power during discharge operation.

Table 10
Performance data for discharging operation.

Parameter	Value
γ_r	0.07594
γ_p	1.424
τ	0.1041
μ	0.512
q_{in} (kJ/kg geothermal water)	365.2
$w_{ejec,net}$ (kJ/kg CO2)	46.88
w_{geo} (kJ/kg geothermal water)	66.75
$\dot{W}_{ejec}$ (kW)	6675
β_{cry} (kg Propane/kg geothermal water)	0.05251
α (kg Propane/kg liquid air)	0.3246
w_{corc} (kJ/kg)	82.94
$\dot{W}_{corc}$ (kW)	1342
q_{ces} (kJ/kg liquid air)	207.7
$\dot{Q}_{ces}$ (kW)	3360
$w_{ces,exp}$ (kJ/kg)	460.7
$\dot{W}_{ces,exp}$ (kW)	7453
w_{ces} (kJ/kg)	543.7
$\dot{W}_{ces}$ (kW)	8794
η_{rt} (%)	41.07
ε_{ces} (%)	60.43

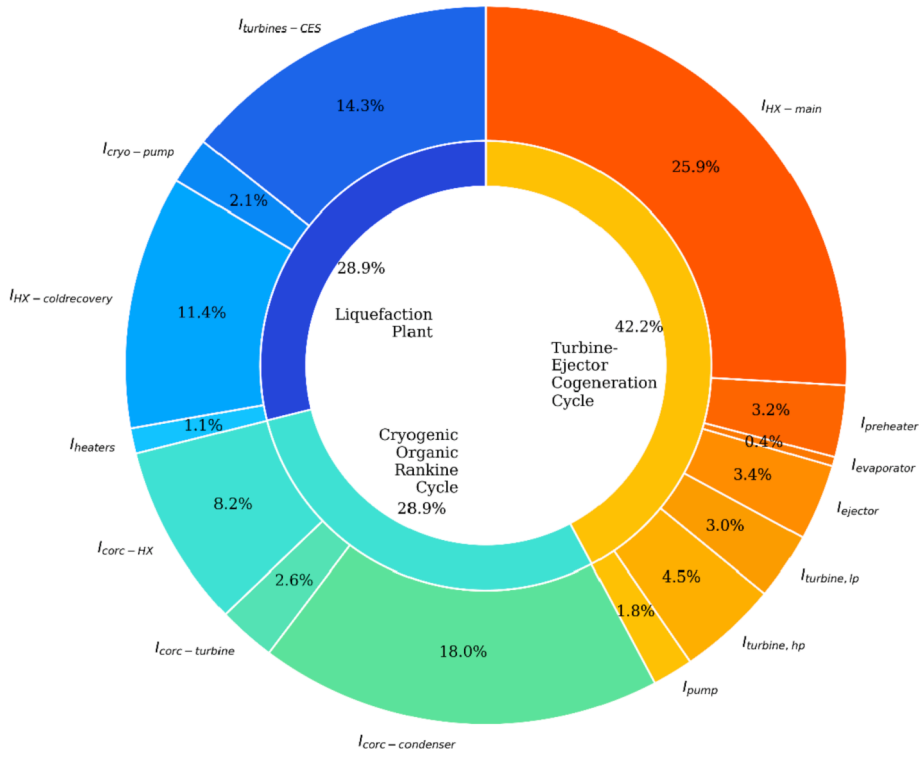

Fig. 9. Proportional irreversibility distribution during discharging operation.

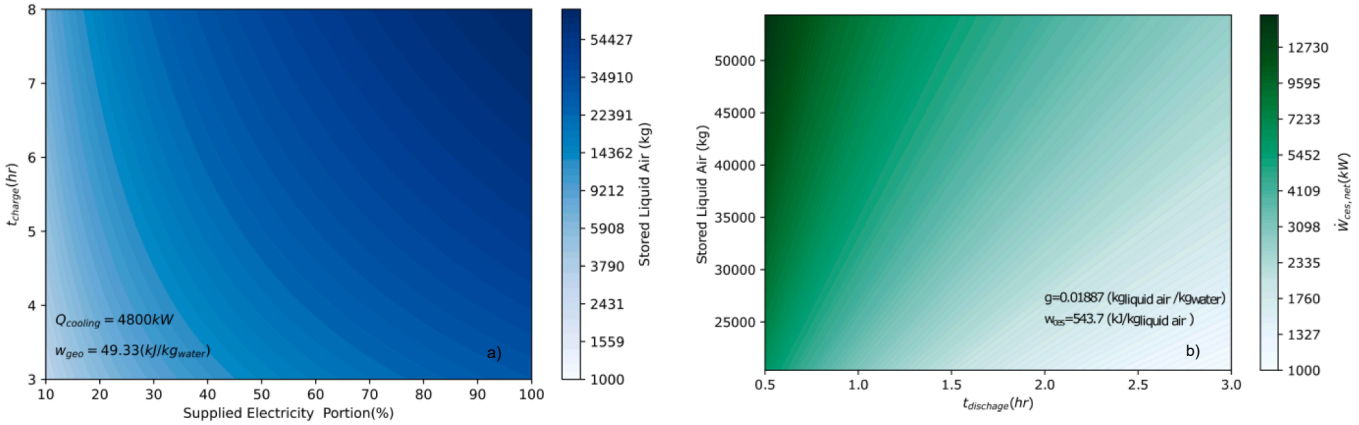

Fig. 10. Variation of a) stored liquid air with supplied electricity portion and charging time b) net power out output from the CES with discharge time and stored liquid amount.

5.1.2. Charging operation

In the charging operation mode, the work output from the turbine ejector cycle is used to liquefy air for 6 h of off-peak period. Thermodynamic states of the working fluids during charging operation period are given in Table 7, based on the state numbers specified in Fig. 2.

Performance data of the whole system during charging operation period are summarized in Table 8. During 6 h of charging operation, the turbine ejector cogeneration cycle produces 49.33 kJ power per kg of geothermal water, while maintaining 4800 kW cooling output. The mass flow ratio diverted to the power section γp is 1.247 and the net power output is 4933 kW. The thermal and exergy efficiencies are 31.0% and 59.4%, respectively.

The liquefaction cycle consumes 1829 kJ energy per unit mass of liquid air. The liquid yield y is 0.2199, which indicates the liquefaction of 21.99% of gaseous air. The mass of liquid air produced per unit of geothermal water *g* is 0.02696 which means 26.96 g liquid air is produced for one kg geothermal water entering the system. 58.234 tons of liquid air are stored during the entire charging period.

The proportional distribution of each component's exergy destruction during charging operation is shown in Fig. 7. The total irreversibility is 6186.5 kW during the charging operation. Among them, 4835.0 kW is originated from the turbine ejector cogeneration cycle, which accounts for 78% of the total exergy destruction. Furthermore, the greatest irreversibility occurs in the main heat exchanger with 2531 kW, this is due to the big temperature difference and misbalance between specific heat values of water and CO_2. The air liquefaction cycle is responsible for the rest of 22% of the total irreversibility corresponding to 1351.4 kW. For the liquefaction cycle, the greatest irreversibility portions come from the compressors and cryo-expander with 8.3% and 7.0%, corresponding to 541.4 kW and 433.9 kW, respectively.

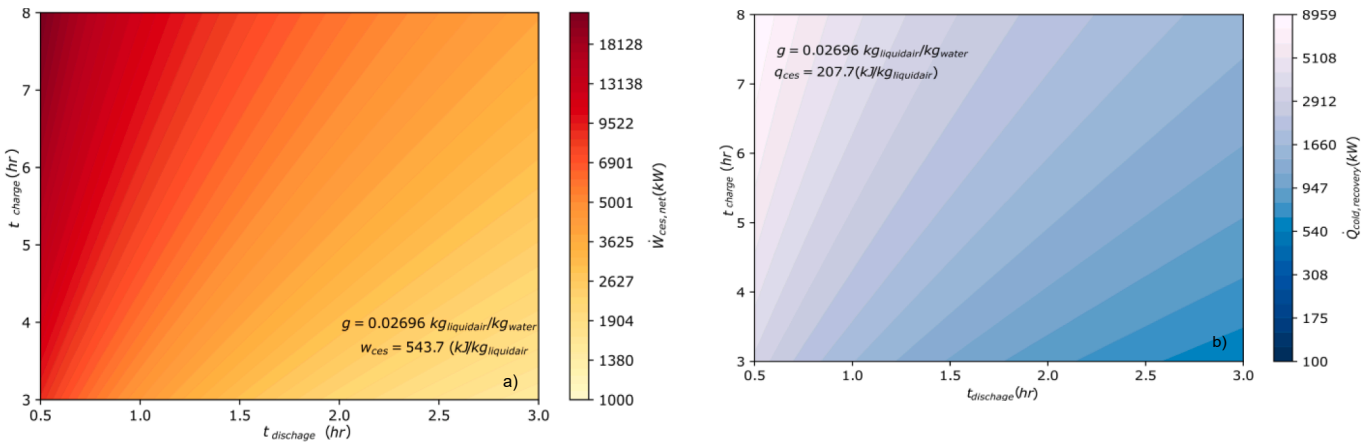

Fig. 11. Variation of the CES power (a) and cooling output (b) rates with different charge and discharge periods.

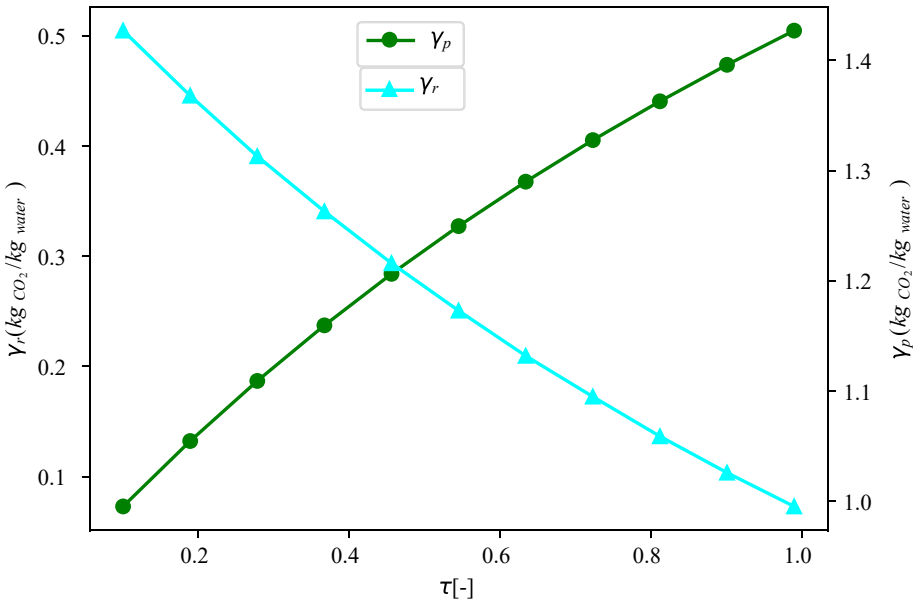

Fig. 12. Effects of turbine mass split ratio on normalized parameters mass flow rate ratio diverted to the power γ_p and cooling γ_r sections.

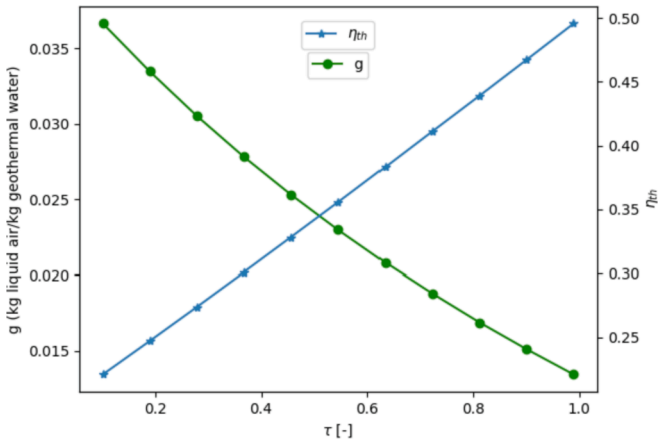

Fig. 13. Effects of turbine mass split ratio on parameter "*g*" and thermal efficiency.

5.1.3. *Discharging operations*

The system is designed to operate in discharge mode at peak time. Thermodynamic properties at each state in this operation mode are determined and given in Table 9. During one hour of discharge operation, all the stored 58.234 tons liquefied air is discharged corresponding to a flow rate of 16.18 kg/s.

The direct liquid air expansion cycle and CORC produce 460.7 kJ and 82.94 kJ work per unit mass of liquefied air respectively. The cold recovery unit supplies 3360 kW cooling capacity while the total cooling demand is 4800 kW. The remaining 1440 kW of cooling demand is provided by the turbine ejector cogeneration cycle. In this case, the turbine mass split ratio τ is reduced to 0.1041 and the net power output of the turbine ejector cogeneration cycle is increased to 6675 kW. In addition to this, the direct liquid air expansion cycle and CORC provide 7453 kW and 1342 kW power, respectively. Therefore, the integrated system supplies 15,470 kW net power which is 3.14 times that produced in normal operation mode, and still provides 4800 kW of cooling during the discharging operation. The distribution of power generation is given in Fig. 8. The turbine ejector cogeneration cycle and cryogenic turbines account for most of the power output with 43% and 48%, respectively, while the cryogenic organic cycle produces 9% of the total power.

In the charging operation, the liquefaction work is 1829 kJ per kg

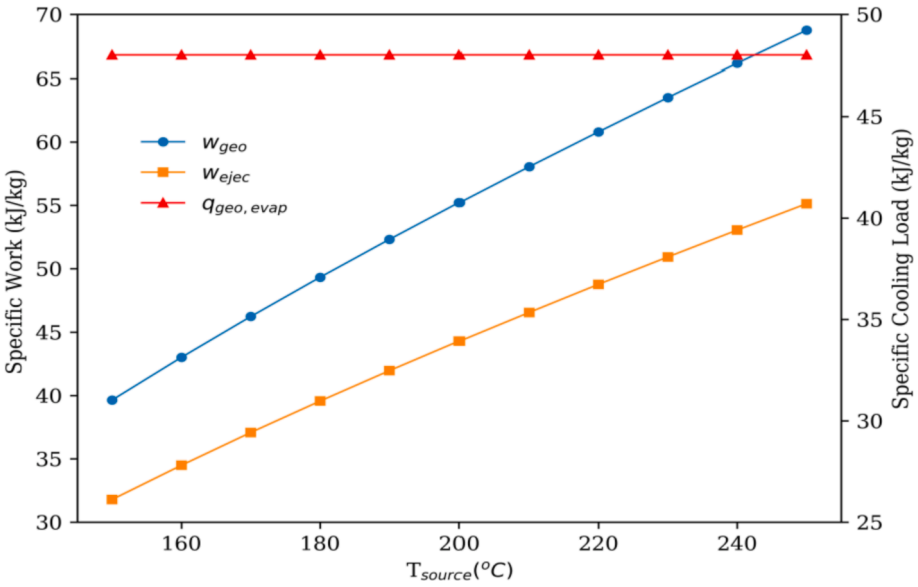

Fig. 14. Effects of source temperature on specific work and specific cooling during charging operation.

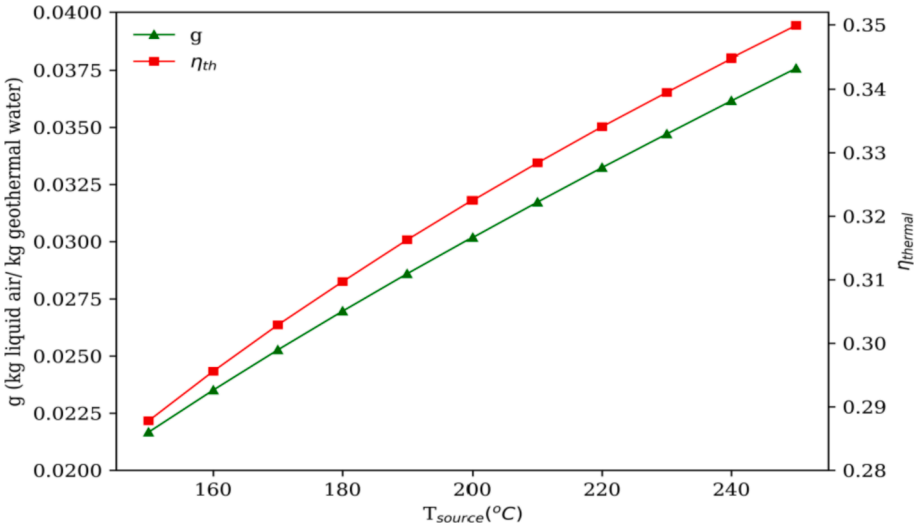

Fig. 15. Effects of source temperature on parameter g and thermal efficiency during charging operation.

liquid air. Using the stored liquid air, 543.7 kJ/kg net work is produced during the discharge operation, 207.7 kJ/kg cold energy is supplied to the district cooling system. Thus, the system round-trip efficiency is 41.07% and the exergy efficiency of cryogenic energy storage is 60.43%. The summary of performance results during the discharge operation is given in Table 10.

During the discharging operation, 10,124 kW exergy is destroyed by the air liquefaction cycle, the CORC and the turbine ejector cogeneration cycle, as shown in Fig. 9. The largest part of irreversibility is from the turbine ejector cogeneration cycle with 4272.7 kW corresponding to 42.2% of the total irreversibility. Similar to the charging operation case, the main heat exchanger is responsible for considerable amount of exergy destruction with 2605 kW, which is 25.9% of the total destructions in the cogeneration cycle. The direct expansion cycle and the CORC cause 2926 kW (28.9%) and 2925.4 kW (28.9%) exergy destructions, respectively. In these two cycles, the condenser of the CORC and the turbines in the liquefaction cycle involve 1825 kW (18%) and 1447 kW (14.3%) irreversibilities, respectively.

5.2. System operation under different scenarios

The developed models can be used to evaluate system performance from geothermal water aspect, the system performance under different charging and discharging periods are investigated. In the presented case study, it's assumed that 100% of electricity generated by the turbine ejector cogeneration cycle in the charging operation mode is supplied to the air liquefaction cycle. In Fig. 10 a), variations of stored liquid air with supplied electricity portion to the liquefaction cycle and different charging operation hours are given. Under the same operating scenario in reference[33], 70% of the system produced electricity is supplied to the liquefaction cycle for 8 h in charging operation mode, 54.4 tons of liquid air can be produced, the system power output is 13,100 kW (Fig. 10b) for one hour discharging period. The case in reference [33] shows the power output in the discharging operation mode is 2.71 times higher than what produced in normal operation mode with the heat source temperature 286 °C, while this study achieves 2.67 times higher than what produced in normal operation mode with the geothermal temperature 180 °C. Therefore, it means the system in this study has the similar performance even though it is driven by the low-grade heat

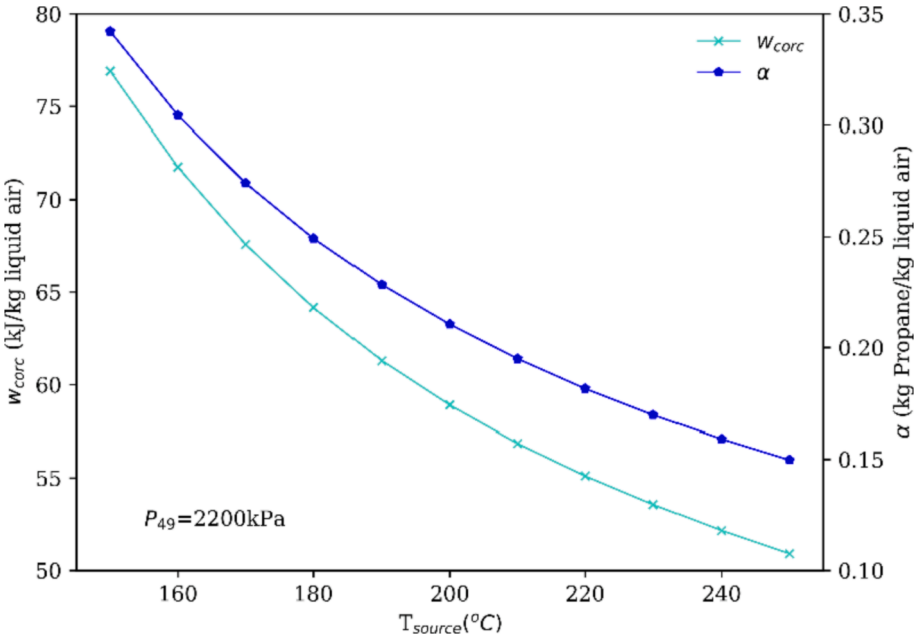

Fig. 16. Effects of source temperature on specific work produced per unit mass of liquid air from the CORC and parameter α.

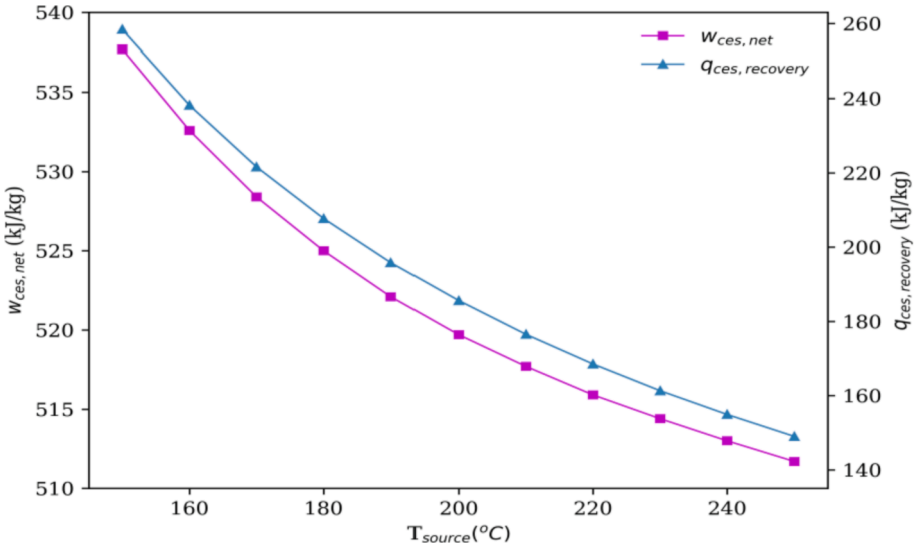

Fig. 17. Effects of source temperature on specific work produced per unit mass of liquid air and specific cold recovery from the CES plant.

source.

Variations of power and cooling output from the CES plant under different charging and discharging operation hours are presented in Fig. 11 a) and b) respectively. For long period of charging operation, more liquid air can be stored, while for short period of discharge operation, high power and cooling output rates from the CES plant can be produced. As the charging period reaches 8 h, the system has the ability to provide up to 24,000 kW power and 9000 kW cooling for 0.5 h discharging period.

5.3. Effects of turbine mass split ratio

The effects of turbine mass split ratio on mass flow rate ratio diverted to the power and cooling sections in the turbine ejector cogeneration cycle are given in Fig. 12. As the turbine mass split ratio increases, more CO_2 is diverted to the ejector's primary nozzle, this also increases the secondary flow rate in the ejector. The mass flow ratio diverted to the cooling section, γ_r, increases from 0 to 0.5046, and the mass flow ratio diverted to the power section decreases from 1.5 to 0.9954 when the turbine mass split ration changes from 0 to 1. It is noted that the mass flow ratio diverted to the cooling section is constrained by the ejector entrainment ratio.

As indicated in Fig. 6, the specific work produced per unit mass of geothermal water decreases with the turbine mass split ratio, and less power is used to liquefy air. When the split ratio changes from 0 to 1, the liquid air produced per unit of geothermal water, parameter g, decreases from 0.03664 to 0.01345, the thermal efficiency increases from 22% to 49% as shown in Fig. 13.

5.4. Effects of geothermal temperature

Heat source temperature is an important parameter for energy production. The variations of the specific power and cooling output with geothermal temperature during charging operation are given in Fig. 14.

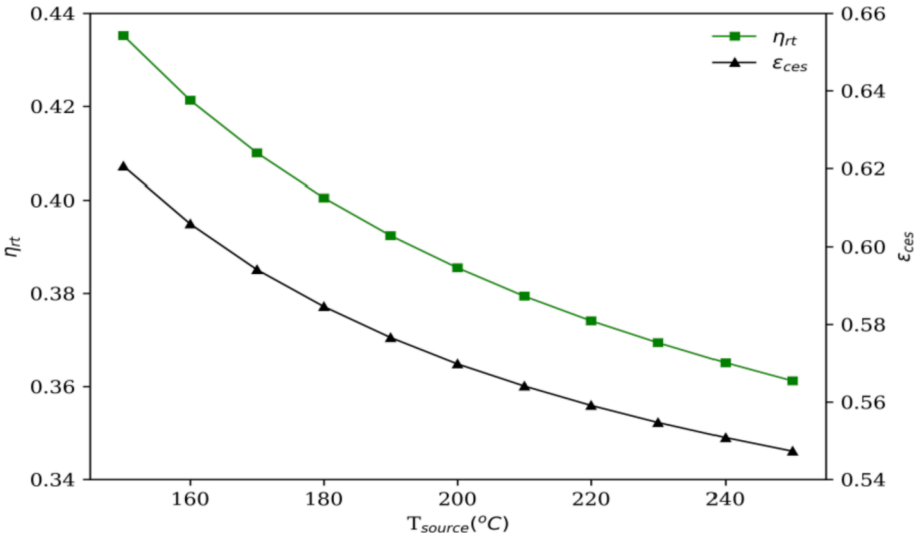

Fig. 18. Effects of source temperature on round trip and exergy efficiencies.

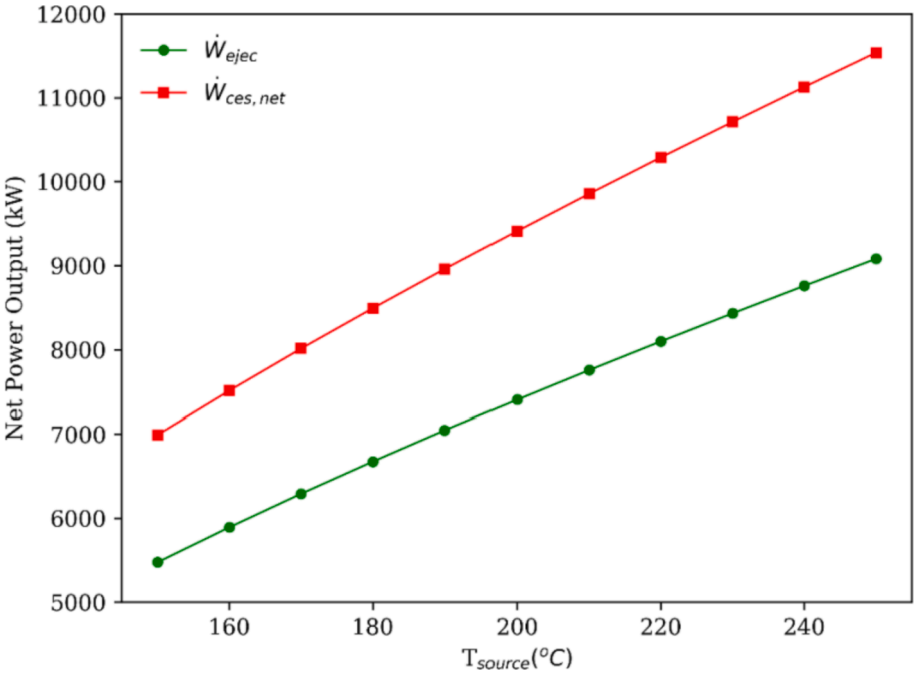

Fig. 19. Effects of source temperature on net power output from the turbine ejector cogeneration cycle and CES during discharge operation.

As the source temperature increases from 150 °C to 250 °C for a constant cooling load of 4800 kW, the turbine mass split ratio decreases from 0.4207 to 0.365 in order to maintain the prescribed ejector outlet pressure. As a result, the specific cooling load, $q_{geo,evap}$, remains at 48 kJ/kg, but the specific work produced by per kg of geothermal water and per kg of CO_2 increase from 39.64 kJ/kg and 31.79 kJ/kg to 68.74 kJ/kg and 55.13 kJ/kg, respectively. With these increases in the specific work produced per kg geothermal water, the liquid air produced per unit of geothermal water, parameter g, increases from 0.02167 to 0.03758. Therefore, more liquid is produced as the geothermal source temperature rises. Also, the thermal efficiency increases from 28.7% to 35% as shown in Fig. 15.

The changes of the specific work produced by the CORC and the unit mass of propane per unit mass of the liquid air, parameter α, with the geothermal temperature are presented in Fig. 16. As more liquid air is released during discharge operation, the parameter α decreases from 0.3421 to 0.1497 when the source temperature increases from 150 °C to 250 °C. As a result, the work produced per unit mass of liquid air decreases from 76.9 to 50.91 kJ/kg in the CORC. As the specific work produced by per unit mass of liquid air decreases, the net work output decreases from 537.7 kJ/kg to 511.7 kJ/kg. Therefore, the recovered cold energy decreases from 258.4 kJ/kg to 149 kJ/kg liquid air as more liquid air is released during discharging operation as indicated in Fig. 17. Consequently, the round trip and exergy efficiencies decrease from 43.52% and 62.06% to 36.12% and 54.73%, respectively as shown in Fig. 18.

The liquid air flow rate increases with g at the high heat source temperature, as a result, the net power output of the CES plant increases from 6991 kW to 11,538 kW as the geothermal temperature varies from 150 °C to 250 °C. During the discharging operation, the available cold of the liquid air can also be utilized in district cooling. For a constant cooling demand, one portion of this demand is supplied by the liquid air,

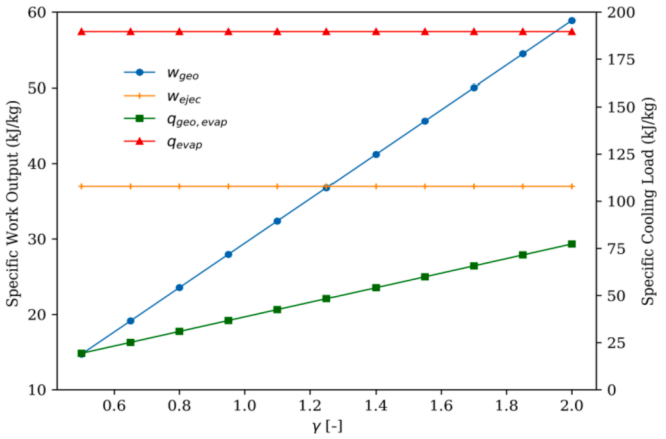

Fig. 20. Effects of parameter γ on specific power and cooling during charging operation.

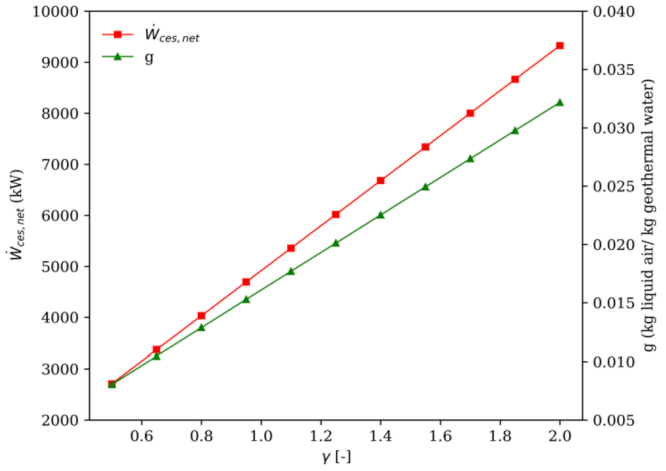

Fig. 21. Effects of parameter γ on net power output from the CES plant and parameter g.

the remaining portion of cooling demand is met by the turbine ejector cogeneration cycle. The turbine mass split ratio decrease as the heat source temperature increases. Consequently, the generated power in the cogeneration cycle increases from 5477 kW to 9081 kW when the geothermal temperature changes from 150 °C to 250 °C, as shown in Fig. 19.

5.5. Effects of system size

The variations of the specific work and cooling load with the normalized mass flow rate γ are presented in Fig. 20. The specific work and cooling load per unit mass of CO_2 remain unchanged while the normalized mass flow rate γ increases from 0.5 to 2. On the other hand, when the parameter γ changes from 0.5 to 1.5, the specific power and cooling output produced per unit mass of geothermal water increase from 14.72 kJ/kg and 19.33 kJ/kg to 58.87 kJ/kg and 77.31 kJ/kg, respectively.

The variations of the power generated from the CES plant and parameter *g* with the normalized mass flow rate γ are shown in Fig. 21. The power is increased from 2709.7 kW to 9326.6 kW and the mass of liquid air produced per unit of geothermal water, parameter g, rises from 0.008045 to 0.03218 kg liquid air per kg geothermal water when the normalized mass flow rate, parameter γ, increases from 0.5 to 2. This can be explained as follows, the liquid air produced per unit mass of geothermal water *g* increases with the normalized mass flow rate γ. The increase in the parameter g affects the net power output because more liquid air is released during charging operation.

The work produced per unit mass of liquid air in the CORC is affected by the normalized mass flow rate, γ, in two ways. Increasing γ leads to a temperature reduction of outlet stream from the main heat exchanger, and thus the low temperature heat is supplied to the CORC, and as the more liquid air is discharged, the specific work produced per unit mass of liquid air in the CORC further reduces from 100.5 kJ/kg to 22.21 kJ/kg as the parameter γ increases from 0.5 to 2 (as displayed in Fig. 22). This leads to a decline in the net specific work of the CES plant.

5.6. System performance justification

The turbine ejector cogeneration cycle produces 4800 kW cooling and 4933 kW power in charging operation mode as indicated in section 5.1.2, all the produced power is used to liquefy air in the air liquefaction cycle. In this operation mode, thermal and exergy efficiencies of the turbine ejector cogeneration cycle are 31.0% and 59.3%, respectively. The liquefaction cycle consumes 1829 kJ/kg per unit mass of air and produces 27 g of liquid air for one kg geothermal water. During 6 h of operation, 58.234 tons of liquid air are produced. During one hour of discharging operation, all liquid air is discharged through the CORC to generate 1342 kW power. The stored air supplied at a rate of 16.18 kg/s provides 70% of the total 4800 kW cooling requirement by cold recovery. The downstream is expanded through two consecutive turbines to produce 7454 kW of additional power output. In the meantime, the turbine ejector cogeneration cycle generates 6675 kW power and supplies the remaining 1440 kW cooling demand. The total net power output is 15,470 kW with 41.07% round trip efficiency, and the exergy efficiency of the cryogenic energy storage is 60.43%. The system performance under various scenarios are investigated, and in overall, the system produces 510–540 kJ/kg liquid air with round trip efficiency in the range of 40–45% and exergy efficiency in the range of 60–65%. In the available literature, some studies demonstrated the similar performance. Tafone et al. [40] proposed a system which has the round trip efficiency in range of 42.60–52.55%. Yao et al. [41] carried out thermodynamic optimization of a combined cooling, heating and power system with compressed air energy storage, and achieved the system exergy efficiency of 53.04%. Bosch et al. [26] designed a stand-alone cryogenic energy storage system operating in cogeneration regime to supply power and cooling with a round trip efficiency of 42%. Zhang et al. [28] developed a cryogenic thermoelectric generator for recovering cryogenic energy, and noted that the overall round trip efficiency is 29% and the combined cooling and power efficiency is 50%. By referencing to these studies, it can be seen that the proposed system exhibits competitive specific work output and exergy efficiency.

6. Conclusions

In this study, a geothermal power and cooling cogeneration system with cryogenic energy storage is proposed, and the synergic operation characteristics are investigated according to the first and second laws of thermodynamics. Parametric analyses are carried out to assess the system performance under different operating modes. Following conclusions can be drawn based on results of this study:

- During 6 h of charging operation, the turbine ejector cogeneration cycle produces 4800 kW cooling to meet the district cooling demand, and 4933 kW power to liquefy air in the air liquefaction cycle, and the cycle produces 27 g of liquid air for one kg geothermal water. During this operation period, the energy and exergy efficiencies of the turbine ejector cogeneration cycle are 31.0% and 59.3%, respectively.
- During one hour of discharging operation, the cryogenic organic Rankine cycle generates 1342 kW power. 58.234 tons of liquid air

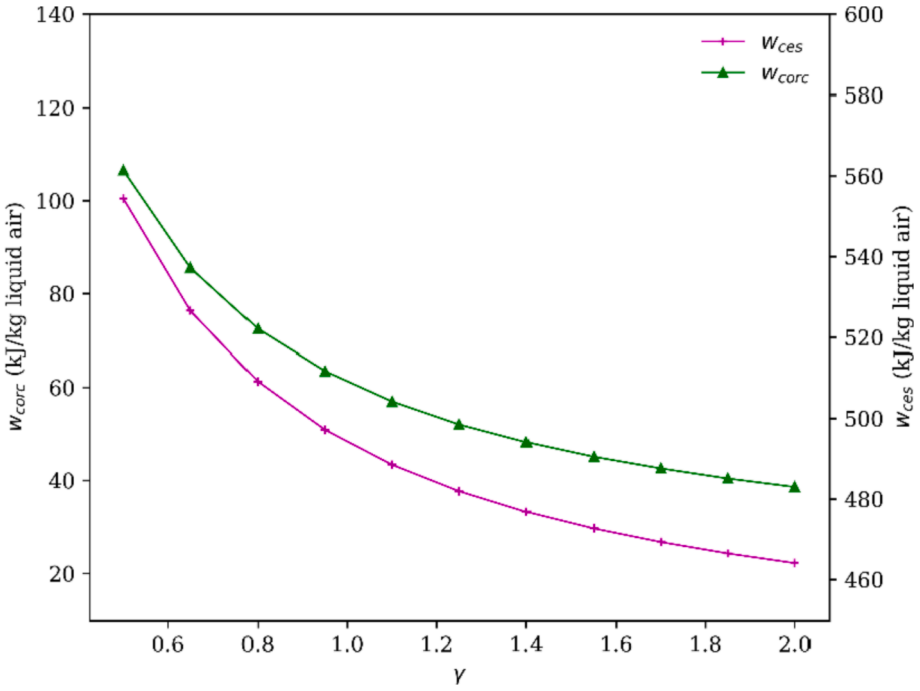

Fig. 22. Effects of parameter γ on specific work output from the CORC and CES plant.

are discharged through the direct expansion cycle to provide 7454 kW of additional power output and meet 70% of the cooling demand.

- During the discharging period, the turbine ejector cogeneration cycle produces 6675 kW power and supplies 30% of the cooling demand. The system total power output is 15,470 kW which is 3.14 times that produced in normal operating mode, the system round trip efficiency is 41.07%, the exergy efficiency of cryogenic energy storage is 60.43%.
- During the discharging operation, the largest irreversibility is in the turbine ejector cogeneration cycle accounting for 42.2%, and the remaining portion of the exergy destructions is shared by direct expansion cycle and CORC with 28.9% for both of them.
- The system power output and cooling supply rates are increased by reducing discharging period. The proposed direct expansion cycle and CORC could supply up to 24,000 kW power and 9000 kW cooling to the district based on 8 h of charging period and half an hour of discharging period.
- Turbine mass split ratio has direct effects on the power and cooling output of the turbine ejector cogeneration cycle. As the mass split ratio decreases from 1 to 0, the specific work per unit mass of geothermal water decreases from 67 kJ/kg to 24 kJ/kg, and the mass of liquid air produced per unit of geothermal water, parameter g, decreases from 0.03664 to 0.01345 (kg liquid air/kg geothermal water).
- Geothermal temperature is an important operating parameter, the higher source temperature, the more power output. The specific work output per unit mass of geothermal water increases from 39 kJ/kg to 68 kJ/kg as the geothermal temperature changes from 150 °C to 250 °C, the integrated system power output increases from 12,300 kW to 20,600 kW.
- Normalized mass flow rate affects the amount of liquefied air, and it is directly related to the system size. As it varies from 0.5 to 2, the mass of liquid air produced per unit of geothermal water increases from 0.008045 to 0.03218 and power output changes from 2700 kW to 9300 kW.

The proposed system can be powered by the other energy sources, such as waste heat, concentrated solar thermal energy. It appears that integration of a cryogenic energy storage into a geothermal power and cooling cogeneration system is a promising solution to fluctuating power and cooling demands. For the future work, the system performance under realistic load state with economic consideration will be investigated.

CRediT authorship contribution statement

Tuğberk Hakan Çetin: Conceptualization, Methodology, Software. **Jie Zhu:** Supervision, Methodology. **Ekrem Ekici:** Visualization, Data curation. **Mehmet Kanoglu:** Supervision, Methodology.

Declaration of Competing Interest

The authors declare that they have no known competing financial interests or personal relationships that could have appeared to influence the work reported in this paper.

Acknowledgement

The financial supports from TUBITAK under 2213/A-Overseas Graduate Scholarship Program and Turkish Ministry of National Education are gratefully acknowledged by Authors.

References

[1] Cao X, Dai X, Liu J. Building energy-consumption status worldwide and the state-of-the-art technologies for zero-energy buildings during the past decade. Energy Build 2016;128:198–213.
[2] Goldstein B, Gounaridis D, Newell JP. The carbon footprint of household energy use in the United States. Proc Natl Acad Sci U S A 2020;117:19122–30. https://doi.org/10.1073/PNAS.1922205117.
[3] Angrisani G, Entchev E, Roselli C, Sasso M, Tariello F, Yaïci W. Dynamic simulation of a solar heating and cooling system for an office building located in Southern Italy. Appl Therm Eng 2016;103:377–90. https://doi.org/10.1016/J.APPLTHERMALENG.2016.04.094.
[4] Werner S. International review of district heating and cooling. Energy 2017;137:617–31.
[5] Gang W, Wang S, Xiao F. District cooling systems and individual cooling systems: Comparative analysis and impacts of key factors. Http://DxDoiOrg/101080/237447312016121447 4 2016;23:241–50. https://doi.org/10.1080/23744731.2016.1214474.

[6] Inayat A, Raza M. District cooling system via renewable energy sources: a review. Renew Sustain Energy Rev 2019;107:360–73.
[7] Kanoğlu M, Çengel YA, Cimbala JM. Fundamentals and applications of renewable energy. 1st ed. New York: McGraw-Hill Education; 2020.
[8] Gang W, Wang S, Xiao Fu, Gao D-c. District cooling systems: technology integration, system optimization, challenges and opportunities for applications. Renew Sustain Energy Rev 2016;53:253–64.
[9] Yilmaz C. Thermodynamic and economic investigation of geothermal powered absorption cooling system for buildings. Geothermics 2017;70:239–48. https://doi.org/10.1016/J.GEOTHERMICS.2017.06.009.
[10] Tugcu A, Arslan O. Optimization of geothermal energy aided absorption refrigeration system—GAARS: A novel ANN-based approach. Geothermics 2017;65:210–21. https://doi.org/10.1016/J.GEOTHERMICS.2016.10.004.
[11] Habibi M, Aligolzadeh F, Hakkaki-Fard A. A techno-economic analysis of geothermal ejector cooling system. Energy 2020;193:116760.
[12] Nami H, Anvari-Moghaddam A. Geothermal driven micro-CCHP for domestic application – Exergy, economic and sustainability analysis. Energy 2020;207:118195. https://doi.org/10.1016/J.ENERGY.2020.118195.
[13] Mosaffa AH, Farshi LG. Thermodynamic and economic assessments of a novel CCHP cycle utilizing low-temperature heat sources for domestic applications. Renew Energy 2018;120:134–50.
[14] Zare V, Rostamnejad Takleh H. Novel geothermal driven CCHP systems integrating ejector transcritical CO2 and Rankine cycles: Thermodynamic modeling and parametric study. Energy Convers Manag 2020;205:112396.
[15] Ipakchi O, Mosaffa AH, Garousi Farshi L. Ejector based CO2 transcritical combined cooling and power system utilizing waste heat recovery: A thermoeconomic assessment. Energy Convers Manag 2019;186:462–72.
[16] Ruiz-Casanova E, Rubio-Maya C, Pacheco-Ibarra JJ, Ambriz-Díaz VM, Romero CE, Wang X. Thermodynamic analysis and optimization of supercritical carbon dioxide Brayton cycles for use with low-grade geothermal heat sources. Energy Convers Manag 2020;216:112978.
[17] Guelpa E, Verda V. Thermal energy storage in district heating and cooling systems: A review. Appl Energy 2019;252:113474. https://doi.org/10.1016/J.APENERGY.2019.113474.
[18] Hamdy S, Morosuk T, Tsatsaronis G. Cryogenics-based energy storage: Evaluation of cold exergy recovery cycles. Energy 2017;138:1069–80.
[19] Vecchi A, Li Y, Mancarella P, Sciacovelli A. Integrated techno-economic assessment of Liquid Air Energy Storage (LAES) under off-design conditions: Links between provision of market services and thermodynamic performance. Appl Energy 2020;262:114589.
[20] Qi M, Park J, Lee I, Moon I. Liquid air as an emerging energy vector towards carbon neutrality: A multi-scale systems perspective. Renew Sustain Energy Rev 2022;159:112201. https://doi.org/10.1016/J.RSER.2022.112201.
[21] Borri E, Tafone A, Romagnoli A, Comodi G. A review on liquid air energy storage: History, state of the art and recent developments. Renew Sustain Energy Rev 2021;137:110572. https://doi.org/10.1016/J.RSER.2020.110572.
[22] O'Callaghan O, Donnellan P. Liquid air energy storage systems: A review. Renew Sustain Energy Rev 2021;146:111113. https://doi.org/10.1016/J.RSER.2021.111113.
[23] Tafone A, Romagnoli A, Li Y, Borri E, Comodi G. Techno-economic analysis of a liquid air energy storage (LAES) for cooling application in hot climates. Energy Procedia 2017;105:4450–7. https://doi.org/10.1016/J.EGYPRO.2017.03.944.
[24] He T, Lv H, Shao Z, Zhang J, Xing X, Ma H. Cascade utilization of LNG cold energy by integrating cryogenic energy storage, organic Rankine cycle and direct cooling. Appl Energy 2020;277:115570. https://doi.org/https://doi.org/10.1016/j.apenergy.2020.115570.
[25] Gao Z, Guo L, Ji W, Xu H, An B, Wang J. Thermodynamic and economic analysis of a trigeneration system based on liquid air energy storage under different operating modes. Energy Convers Manag 2020;221:113184. https://doi.org/https://doi.org/10.1016/j.enconman.2020.113184.
[26] Nuñez Bosch OM, Martins de Oliveira Júnior M, Ponce Arrieta FR, Magalhães Ferreira RA, Pereira Porto M. Thermodynamic assessment of cryogenic energy storage (CES) systems in cogeneration regime. Energy Convers Manag 2021;245:114552. https://doi.org/10.1016/J.ENCONMAN.2021.114552.
[27] Mugnini A, Coccia G, Polonara F, Arteconi A. Potential of district cooling systems: A case study on recovering cold energy from liquefied natural gas vaporization. Energies 2019;12(15):3027.
[28] Zhang T, She X, You Z, Zhao Y, Fan H, Ding Y. Cryogenic thermoelectric generation using cold energy from a decoupled liquid air energy storage system for decentralised energy networks. Appl Energy 2022;305:117749. https://doi.org/10.1016/J.APENERGY.2021.117749.
[29] Vutukuru R, Pegallapati AS, Maddali R. Thermodynamic studies on a solar assisted transcritical CO2 based tri-generation system with an ejector for dairy applications. Int J Refrig 2019;108:113–23. https://doi.org/10.1016/J.IJREFRIG.2019.08.031.
[30] DOWTHERM^{TM} T Heat Transfer Fluid | Dow Inc. n.d. https://www.dow.com/en-us/pdp.dowtherm-t-heat-transfer-fluid.50720z.html (accessed September 3, 2021).
[31] Cetin TH, Kanoglu M, Bedir F. Integration of cryogenic energy storage and cryogenic organic cycle to geothermal power plants. Geothermics 2020;87:101830.
[32] Wang J, Dai Y, Sun Z. A theoretical study on a novel combined power and ejector refrigeration cycle. Int J Refrig 2009;32:1186–94. https://doi.org/https://doi.org/10.1016/j.ijrefrig.2009.01.021.
[33] Li Y, Cao H, Wang S, Jin Yi, Li D, Wang X, et al. Load shifting of nuclear power plants using cryogenic energy storage technology. Appl Energy 2014;113:1710–6.
[34] Cengel YA, Boles MA, Kanoglu M. Thermodynamics: an engineering approach. 2019.
[35] Zhang W, Xue X, Liu F, Mei S. Modelling and experimental validation of advanced adiabatic compressed air energy storage with off-design heat exchanger. IET Renew Power Gener 2020;14:389–98. https://doi.org/10.1049/IET-RPG.2019.0652.
[36] Wark 1927- K. Advanced thermodynamics for engineers. New York : McGraw-Hill, [1995] ©1995; n.d.
[37] Yildiz A, Güngör A. Energy and exergy analyses of space heating in buildings. Appl Energy 2009;86(10):1939–48.
[38] Cetin TH, Kanoglu M, Yanikomer N. Cryogenic energy storage powered by geothermal energy. Geothermics 2019;77:34–40.
[39] Arbel A, Shklyar A, Hershgal D, Barak M, Sokolov M. Ejector irreversibility characteristics. J Fluids Eng 2003;125:121–9. https://doi.org/10.1115/1.1523067.
[40] Tafone A, Borri E, Comodi G, van den Broek M, Romagnoli A. Liquid air energy storage performance enhancement by means of organic rankine cycle and absorption chiller. Appl Energy 2018;228:1810–21.
[41] Yao E, Wang H, Wang L, Xi G, Maréchal F. Multi-objective optimization and exergoeconomic analysis of a combined cooling, heating and power based compressed air energy storage system. Energy Convers Manag 2017;138:199–209.